

Consistency of Gauged Two Higgs Doublet Model: Gauge Sector

Cheng-Tse Huang¹, Raymundo Ramos²,

Van Que Tran^{2,3}, Yue-Lin Sming Tsai^{2,4} and Tzu-Chiang Yuan²

¹*Interdisciplinary Program of Sciences,*

National Tsing Hua University, Hsinchu 30013, Taiwan

²*Institute of Physics, Academia Sinica, Nangang, Taipei 11529, Taiwan*

³*School of Physics, Nanjing University, Nanjing 210093, China*

⁴*Key Laboratory of Dark Matter and Space Astronomy,*

Purple Mountain Observatory, Chinese Academy of Sciences, Nanjing 210008, China

(Dated: June 19, 2019)

We study the constraints on the new parameters in the gauge sector of gauged two Higgs doublet model using the electroweak precision test data collected from the Large Electron Positron Collider (LEP) at and off the Z -pole as well as the current Drell-Yan and high-mass dilepton resonance data from the Large Hadron Collider (LHC). Impacts on the new parameters by the projected sensitivities of various electroweak observables at the Circular Electron Positron Collider (CEPC) proposed to be built in China are also discussed. We also clarify why the Stüeckelberg mass M_Y for the hypercharge $U(1)_Y$ is set to be zero in the model by showing that it would otherwise lead to the violation of the standard charge assignments for the elementary quarks and leptons when they couple to the massless photon.

I. INTRODUCTION

The discovery of the 125 GeV scalar boson identified as the Higgs boson in the Standard Model (SM) [1–4] suggested that the simple Higgs mechanism [5–7] for electroweak symmetry breaking proposed by Weinberg [3] and Salam [4] is the choice by *nature*. Both Run I and Run II data collected by the two experimental groups ATLAS and CMS at the Large Hadron Collider (LHC) reveal no significant deviations from the SM predictions. Alternative models for electroweak symmetry breaking like technicolor or composite Higgs models are arguably more elegant but necessarily more complicated. Simplicity seems to be more superior over other criterion like complexity or elegance for model buildings.

Nevertheless experimental observations of neutrino oscillations imply there must be new physics beyond the SM to account for the minuscule masses of neutrinos. Missing mass problem and cosmic acceleration of our universe also suggested the introduction of dark matter (DM) [8] and dark energy [9]. The standard Λ CDM model of cosmology [10] consists of the SM of particle physics plus two new ingredients, namely the cold dark matter, which can be the weakly interacting massive particle predicted by many new particle physics models, and a tiny positive cosmological constant at the present time in the Einstein’s field equation for gravity, which can be mimicked by numerous models of dark energy. Many models of dark matter and neutrino masses require extension not only of the simple Higgs sector but sometimes also the electroweak gauge sector of the SM as well. Moreover, models of dark energy are often represented by new scalar field with equation of state that can provide negative pressure in order to explain the cosmic acceleration at late times.

Thus extension of the SM in one way or the other seems necessary if one wants to solve the above puzzles in the neutrino sector and in cosmology. At the same time, one should be open-minded that there might be other approaches other than

particle physics to answer some of these questions and remembering that *nature* is the ultimate arbiter of all theoretical imaginations.

The gauged two Higgs doublet model (G2HDM) proposed in [11] was motivated partly by the inert Higgs doublet model (IHDM) [12–15] of dark matter. IHDM is a variant of the general 2HDM [16] with an imposed discrete Z_2 symmetry on the scalar potential and the Yukawa couplings such that one of the Higgs doublets is odd and become a scalar dark matter candidate. Dangerous tree level flavor changing neutral current (FCNC) interactions in the Yukawa couplings, generally presence in the general 2HDM, are also eliminated by this discrete symmetry. Due to its relatively simple extension of the SM, many detailed analysis of IHDM had been done in the literature [17–26]. In G2HDM, the discrete Z_2 symmetry in IHDM was not enforced. Instead the two Higgs doublets H_1 and H_2 are grouped into a two-dimensional irreducible representation $H = (H_1, H_2)^T$ of a new gauge group $SU(2)_H$. A priori there is no need to impose the discrete Z_2 symmetry in G2HDM. Once we write down all renormalizable interactions for G2HDM, this discrete symmetry emerges as an accidental symmetry automatically. Tree level flavor changing neutral current (FCNC) interaction in the Higgs-Yukawa couplings are also absence naturally for the SM fermions. As long as one does not break this symmetry spontaneously, which might lead to the domain wall problem in early universe, the H_2 doublet is naturally an inert Higgs doublet and can play some role in dark matter physics. It is more satisfactory to have a global discrete symmetry like the Z_2 parity that guarantees the stability of dark matter embedded into a local symmetry. Indeed there exists theoretical arguments showing that global continuous or discrete symmetries are not compatible with quantum gravity [27, 28]. Detailed analysis of the complex scalar dark matter physics in G2HDM will be presented in a forthcoming paper [29].

The construction of G2HDM in [11] involves extension of both the Higgs and gauge sector of the SM which we will discuss shortly in the next section. Several

phenomenological implications of G2HDM had been explored in [30, 31, 38, 39]. In particular, we have studied recently in details the theoretical and phenomenological constraints on the scalar sector [31].

We note that the 2HDM augmented with an extra local abelian $U(1)_X$ has been discussed in the literature [32–37] to address neutrino masses, dark matter and to avoid FCNC interactions at the tree level.

As mentioned before, all experimental data are in line with SM predictions. The extended gauge sector of G2HDM must be challenged by electroweak precision test (EWPT) data obtained previously at LEP-I and LEP-II as well as current data at the LHC. Constraints must be imposed on the new parameters in the extended gauge sector of G2HDM. The main purpose of this work is to study these constraints on the gauge sector systematically in analogous to previous analysis [31] done for the scalar sector. It is also interesting to address the sensitivities of these new parameters at the future colliders.

The contents of this paper is organized as follows: In the next Sec. II, we review the G2HDM and highlight some of its crucial features of the gauge sector relevant most to this work. Sec. III discusses the experimental constraints, including the electroweak precision test constraints at and off the Z -pole at LEP, Drell-Yan data from on-shell decay of the Z boson at the LHC, and the full LHC Run II data from the high-mass dilepton resonance of an extra neutral gauge boson Z' . Sec. IV contains our numerical results from the profile likelihood analysis. We also study future sensitivities of the new parameters in future experiments, in particular for the Circular Electron Positron Collider (CEPC) [40] proposed/debated to be built in China. Finally, we summarize and conclude in Sec. V. In Appendix A we present the formulas for the mixing angles among the three massive neutral gauge bosons in G2HDM in terms of the fundamental parameters in the Lagrangian of the model. The dominant two-body decay widths for the two new neutral gauge bosons are

discussed in Appendix B.

II. G2HDM SET UP

In this section, we will start with a brief review for the set-up of G2HDM [11] by specifying its particle content (Sec. II A) and then write down the mass spectrum of the neutral gauge bosons (Sec. II B) and their interactions with the SM fermions (Sec. II C) in the model. Along the way, we will discuss some peculiar effects for nonzero Stüeckelberg mass M_Y associated with the hypercharge $U(1)_Y$.

A. Particle Content

The particle content of G2HDM is listed in Table I ¹. Besides the two Higgs doublets H_1 and H_2 combining to form $H = (H_1, H_2)^T$ in the fundamental representation of an extra $SU(2)_H$, we introduced a triplet Δ_H and a doublet Φ_H of this new gauge group. However Δ_H and Φ_H are singlets under the electroweak SM gauge group $SU(2)_L \times U(1)_Y$. Only H carries both quantum numbers of the $SU(2)_L$ and $SU(2)_H$.

There are different ways of introducing new heavy fermions in the model but we choose a simple realization: the heavy fermions together with the SM right-handed fermions comprise $SU(2)_H$ doublets, while the SM left-handed doublets are singlets under $SU(2)_H$. We note that heavy right-handed neutrinos paired up with a mirror charged leptons forming $SU(2)_L$ doublets was suggested before in the mirror fermion model [41]. To render the model anomaly-free, four additional chiral (left-handed) fermions for each generation, all singlets under both $SU(2)_L$ and $SU(2)_H$, are included. For the Yukawa interactions that couple among the fermions and scalars

¹ $u_L^H, d_L^H, \nu_L^H, e_L^H$ in the table were denoted as $\chi_u, \chi_d, \chi_\nu, \chi_e$ respectively in [11].

Fields	Spin	$SU(3)_C$	$SU(2)_L$	$SU(2)_H$	$U(1)_Y$	$U(1)_X$
$H = (H_1 \ H_2)^T$	0	1	2	2	$\frac{1}{2}$	1
$\Delta_H = \begin{pmatrix} \Delta_{3/2} & \Delta_p/\sqrt{2} \\ \Delta_m/\sqrt{2} & -\Delta_{3/2} \end{pmatrix}$	0	1	1	3	0	0
$\Phi_H = (\Phi_1 \ \Phi_2)^T$	0	1	1	2	0	1
$Q_L = (u_L \ d_L)^T$	$\frac{1}{2}$	3	2	1	$\frac{1}{6}$	0
$U_R = (u_R \ u_R^H)^T$	$\frac{1}{2}$	3	1	2	$\frac{2}{3}$	1
$D_R = (d_R^H \ d_R)^T$	$\frac{1}{2}$	3	1	2	$-\frac{1}{3}$	-1
u_L^H	$\frac{1}{2}$	3	1	1	$\frac{2}{3}$	0
d_L^H	$\frac{1}{2}$	3	1	1	$-\frac{1}{3}$	0
$L_L = (\nu_L \ e_L)^T$	$\frac{1}{2}$	1	2	1	$-\frac{1}{2}$	0
$N_R = (\nu_R \ \nu_R^H)^T$	$\frac{1}{2}$	1	1	2	0	1
$E_R = (e_R^H \ e_R)^T$	$\frac{1}{2}$	1	1	2	-1	-1
ν_L^H	$\frac{1}{2}$	1	1	1	0	0
e_L^H	$\frac{1}{2}$	1	1	1	-1	0
$g_\mu^a (a = 1, \dots, 8)$	1	8	1	1	0	0
$W_\mu^i (i = 1, 2, 3)$	1	1	3	1	0	0
$W_\mu^h (i = 1, 2, 3)$	1	1	1	3	0	0
B_μ	1	1	1	1	0	0
X_μ	1	1	1	1	0	0

TABLE I. Particle content and their quantum number assignments in G2HDM.

in G2HDM, we refer our readers to [11] for more details, since they are not relevant to this work.

To avoid some unwanted pieces in the scalar potential and Yukawa couplings, we

require the matter fields to carry extra local $U(1)_X$ charges. Thus the complete gauge groups in G2HDM consist of $SU(3)_C \times SU(2)_L \times U(1)_Y \times SU(2)_H \times U(1)_X$. Apart from the matter content of G2HDM, there also exist the gauge bosons corresponding to the SM and the extra gauge groups.

The salient features of G2HDM are: (i) it is free of gauge and gravitational anomalies; (ii) renormalizable; (iii) without resorting to an ad-hoc Z_2 symmetry, an inert Higgs doublet H_2 can be naturally realized, providing a DM candidate; (iv) due to the nonabelian $SU(2)_H \times U(1)_X$ gauge symmetry, dangerous FCNC interactions are absent at tree level for the SM sector; (v) the VEV of the triplet can trigger $SU(2)_L$ symmetry breaking while that of Φ_H provides a mass to the new fermions through $SU(2)_H$ -invariant Yukawa couplings; *etc.*

B. Neutral Gauge Boson Masses

Consider the interaction basis $\{B, W^3, W'^3, X\}$ for the neutral gauge bosons and denote their mass eigenstates as $\{A, Z_1, Z_2, Z_3\}$. After spontaneous symmetry breaking, the 4×4 mass matrix in the interaction basis of $\{B, W^3, W'^3, X\}$ is given by [11]

$$\mathcal{M}_{\text{gauge}}^2 = \begin{pmatrix} \frac{g'^2 v^2}{4} + M_Y^2 & -\frac{g' g v^2}{4} & \frac{g' g_H v^2}{4} & \frac{g' g_X v^2}{2} + M_X M_Y \\ -\frac{g' g v^2}{4} & \frac{g^2 v^2}{4} & -\frac{g g_H v^2}{4} & -\frac{g g_X v^2}{2} \\ \frac{g' g_H v^2}{4} & -\frac{g g_H v^2}{4} & \frac{g_H^2 (v^2 + v_\Phi^2)}{4} & \frac{g_H g_X (v^2 - v_\Phi^2)}{2} \\ \frac{g' g_X v^2}{2} + M_X M_Y & -\frac{g g_X v^2}{2} & \frac{g_H g_X (v^2 - v_\Phi^2)}{2} & g_X^2 (v^2 + v_\Phi^2) + M_X^2 \end{pmatrix}. \quad (1)$$

Here g , g' , g_H and g_X denote the gauge couplings of $SU(2)_L$, $U(1)_Y$, $SU(2)_H$ and $U(1)_X$ respectively; v and v_Φ are the vacuum expectation values (VEVs) of H_1 and Φ_H respectively; M_X and M_Y are the Stüeckelberg masses for the two abelian $U(1)_X$ and $U(1)_Y$ respectively. We note that v_Δ the VEV of the triplet Δ_H does not enter into the neutral gauge boson mass matrix. This is unlike the case of scalar boson

mass matrix analyzed in [31] which involves all three VEVs, v , v_H and v_Δ . The matrix $\mathcal{M}_{\text{gauge}}^2$ in Eq. (1) is real and symmetric and thus can be diagonalized by a 4×4 orthogonal rotation matrix that we will denote as $\mathcal{O}^{4 \times 4}$

$$(\mathcal{O}^{4 \times 4})^T \cdot \mathcal{M}_{\text{gauge}}^2 \cdot \mathcal{O}^{4 \times 4} = \text{diag}(0, M_{Z_1}^2, M_{Z_2}^2, M_{Z_3}^2), \quad (2)$$

where $M_{Z_1}^2 < M_{Z_2}^2 < M_{Z_3}^2$. The zero mass state is naturally identified as the photon.

Some comments on the Stüeckelberg masses M_X and M_Y are in order here. It has been demonstrated in [42] that for the extension of SM with a Stüeckelberg mass M_Y for the hypercharge $U(1)_Y$, there exists a plethora of new physical effects. Notably, besides the photon obtaining a mass, neutrinos will couple to the photon and charged leptons will have axial vector couplings with the photon. Nevertheless, the Stüeckelberg extension of the SM doesn't spoil renormalizability of the model. All these new effects are proportional to M_Y . Experimentally, the photon mass upper bound deduced from modeling the solar wind in magnetohydrodynamics is $m_\gamma < 1 \times 10^{-18}$ eV [43], which implies M_Y must be very tiny too. If individual Stüeckelberg mechanism is introduced for each of the two $U(1)$ s factors in G2HDM, the photon will in general obtain nonzero mass and many results obtained in [42] apply as well. In [11], we followed [44–47] in which only one Stüeckelberg field was introduced for the two factors of $U(1)$ s to implement the Stüeckelberg mechanism. The matrix $\mathcal{M}_{\text{gauge}}^2$ thus obtained given in Eq. (1) has zero determinant and a massless photon can always be realized for arbitrary values of the Stüeckelberg masses M_X and M_Y .

In the next subsection, we will show that with a nonzero M_Y the electric charge assignments of the SM fermions and their heavy partners in G2HDM will no longer be standard but instead receive milli-charge corrections like those discussed in [42]. In particular, neutrinos will couple to the photon and all fermions also have axial vector couplings with the photon at tree level. These peculiar effects depend on M_Y through the mixing matrix elements and hence necessarily small. Thus, we

have strong theoretical motivation to set $M_Y = 0$ in what follows to avoid these unpleasant features. For an analysis with both M_X and M_Y nonzero in a Stüeckelberg $U(1)_X$ extension of the SM that maintains the standard QED interaction for the SM fermions, see [48–50]. The main reason why the photon-fermion couplings in G2HDM are in general different from these previous works is due to the presence of the extra gauge group $SU(2)_H$ whereas there is only one extra abelian group $U(1)_X$ in [48–50].

Setting $M_Y = 0$ in G2HDM will simplify $\mathcal{M}_{\text{gauge}}^2$ and allows us to write the rotation matrix in the following product form

$$\mathcal{O}_{M_Y=0}^{4 \times 4} = \begin{pmatrix} c_W & -s_W & 0 & 0 \\ s_W & c_W & 0 & 0 \\ 0 & 0 & 1 & 0 \\ 0 & 0 & 0 & 1 \end{pmatrix} \cdot \begin{pmatrix} 1 & 0 & 0 & 0 \\ 0 & & & \\ 0 & \mathcal{O} & & \\ 0 & & & \end{pmatrix}, \quad (3)$$

where c_W and s_W represent $\cos \theta_W$ and $\sin \theta_W$ respectively, with θ_W being the Weinberg angle defined by

$$e^{\text{SM}} \equiv g \sin \theta_W = g' \cos \theta_W = \frac{gg'}{\sqrt{g^2 + g'^2}}. \quad (4)$$

It is obvious that the matrix $\mathcal{O}_{M_Y=0}^{4 \times 4}$ in Eq. (3) is just the product of the SM gauge rotation matrix made into a 4×4 matrix, called $\mathcal{O}_{\text{SM}}^{4 \times 4}$, times a general 3×3 orthogonal rotation matrix \mathcal{O} which was also converted to a 4×4 matrix. After applying the rotation $\mathcal{O}_{\text{SM}}^{4 \times 4}$ to $\mathcal{M}_{\text{gauge}}^2(M_Y = 0)$, the result is

$$\mathcal{O}_{\text{SM}}^{4 \times 4 \text{T}} \cdot \mathcal{M}_{\text{gauge}}^2(M_Y = 0) \cdot \mathcal{O}_{\text{SM}}^{4 \times 4} = \begin{pmatrix} 0 & 0 & 0 & 0 \\ 0 & M_{Z\text{SM}}^2 & -\frac{g_H v}{2} M_{Z\text{SM}} & -g_X v M_{Z\text{SM}} \\ 0 & -\frac{g_H v}{2} M_{Z\text{SM}} & \frac{g_H^2 (v^2 + v_\Phi^2)}{4} & \frac{g_X g_H (v^2 - v_\Phi^2)}{2} \\ 0 & -g_X v M_{Z\text{SM}} & \frac{g_X g_H (v^2 - v_\Phi^2)}{2} & g_X^2 (v^2 + v_\Phi^2) + M_X^2 \end{pmatrix}, \quad (5)$$

where $M_{Z^{\text{SM}}} = v\sqrt{g^2 + g'^2}/2$ is the mass of the Z boson in the SM. We can consider the vanishing (1,1) element to be the mass of the photon eigenstate A_μ . Furthermore, according to Eqs. (2) and (3), the remaining 3×3 matrix formed by the non-vanishing elements above is diagonalized by the orthogonal matrix \mathcal{O} . In particular, one can parametrize \mathcal{O} in terms of the following Tait-Bryan representation

$$\mathcal{O} = \begin{pmatrix} c_\psi c_\phi - s_\theta s_\phi s_\psi & -c_\theta s_\phi & s_\psi c_\phi + s_\theta s_\phi c_\psi \\ c_\psi s_\phi + s_\theta c_\phi s_\psi & c_\theta c_\phi & s_\psi s_\phi - s_\theta c_\phi c_\psi \\ -c_\theta s_\psi & s_\theta & c_\theta c_\psi \end{pmatrix}, \quad (6)$$

where s_x and c_x stand for sine and cosine with the rotation angle $x = \phi, \theta, \psi$ respectively. As shown in Appendix A, these rotation angles can be represented as

$$\tan(\phi) = \frac{-g_H v M_{Z^{\text{SM}}} (M_X^2 - M_{Z_2}^2 + 2g_X^2 v_\Phi^2)}{2 \left(M_{Z_2}^4 - (M_{Z^{\text{SM}}}^2 + M_X^2 + (v^2 + v_\Phi^2) g_X^2) M_{Z_2}^2 + M_{Z^{\text{SM}}}^2 (M_X^2 + g_X^2 v_\Phi^2) \right)}, \quad (7)$$

$$\tan(\theta) = \frac{-g_X (M_{Z_2}^2 (v^2 - v_\Phi^2) + M_{Z^{\text{SM}}}^2 v_\Phi^2)}{v M_{Z^{\text{SM}}} (M_X^2 - M_{Z_2}^2 + 2g_X^2 v_\Phi^2)} \sin \phi, \quad (8)$$

$$\cot(\psi) = \frac{g_H (M_{Z_1}^2 - M_X^2 - 2g_X^2 v_\Phi^2) \cos \theta}{g_X (g_H^2 v_\Phi^2 - 2M_{Z_1}^2)} \frac{\cos \theta}{\sin \phi} - \sin \theta \cot \phi. \quad (9)$$

It is easy to see that taking the limits of g_H and g_X go to 0, the non-vanishing 3×3 block matrix in Eq. (5) becomes $\text{Diag}(M_{Z^{\text{SM}}}^2, 0, M_X^2)$. Thus the rotation matrix \mathcal{O} must be identity. This can be realized by setting ϕ, θ and ψ to be zeros which can be derived from Eqs. (7), (8) and (9).

We note that if one sets M_X to zero, the mass matrix in the right-handed side of Eq. (5) is symmetric under the interchange of $g_H/2 \leftrightarrow g_X$.

After the rotation matrix \mathcal{O} is found, the Z_i mass eigenstates where i runs from 1 to 3 are given by

$$(Z_1, Z_2, Z_3)^{\text{T}} = \mathcal{O}^{\text{T}} \cdot (Z^{\text{SM}}, W'^3, X)^{\text{T}}. \quad (10)$$

The composition Z^{SM} , W^3 and X of the Z_i mass eigenstate is given by \mathcal{O}_{1i}^2 , \mathcal{O}_{2i}^2 , and \mathcal{O}_{3i}^2 , respectively. In general, the Z -pole can be any one of the Z_i depending on which one is actually closer to the pole by the underlying parameter choices in G2HDM. In our analysis, we will consider there is always at least one extra neutral gauge boson heavier than the Z -pole.

C. Neutral Gauge Current Interactions

The part of the Lagrangian that contains the interaction of the Z_i with visible matter in G2HDM is

$$\mathcal{L}_N = g_M \sum_f \sum_{i=1}^3 \bar{f} \gamma_\mu \left[\left(v_f^{(i)} - \gamma_5 a_f^{(i)} \right) Z_i^\mu \right] f, \quad (11)$$

where $g_M = \sqrt{g^2 + g'^2}/2$. The $v_f^{(i)}$ and $a_f^{(i)}$ factors are given by ($M_Y \neq 0$)

$$v_f^{(i)} = (c_W \mathcal{O}_{2,i+1}^{4 \times 4} - s_W \mathcal{O}_{1,i+1}^{4 \times 4}) T_f^3 + 2Q_f s_W \mathcal{O}_{1,i+1}^{4 \times 4} + \frac{1}{\sqrt{g^2 + g'^2}} (X_R g_X \mathcal{O}_{4,i+1}^{4 \times 4} + T_{f_R}^{3H} g_H \mathcal{O}_{3,i+1}^{4 \times 4}), \quad (12)$$

$$a_f^{(i)} = (c_W \mathcal{O}_{2,i+1}^{4 \times 4} - s_W \mathcal{O}_{1,i+1}^{4 \times 4}) T_f^3 - \frac{1}{\sqrt{g^2 + g'^2}} (X_R g_X \mathcal{O}_{4,i+1}^{4 \times 4} + T_{f_R}^{3H} g_H \mathcal{O}_{3,i+1}^{4 \times 4}). \quad (13)$$

Here T_f^3 is the $SU(2)_L$ isospin charge and Q_f is the electric charge in units of e^{SM} for the SM fermion f where e^{SM} is given by Eq. (4). They are related to the $U(1)_Y$ hypercharge by the standard formula $Q_f^{\text{SM}} = T_f^3 + Y_f$. The charges due to the new gauge symmetries are X_R as the $U(1)_X$ charge of the corresponding f_R and $T_{f_R}^{3H}$ is the $SU(2)_H$ analogous of the $SU(2)_L$ isospin T^3 again for the corresponding f_R . We simply define $T_{f_R}^{3H} = \pm 1/2$ depending on f_R belongs to the upper or lower component of an $SU(2)_H$ doublet.

For the photon-fermion couplings in G2HDM, we obtain

$$\mathcal{L}_\gamma = -e^{\text{SM}} \sum_f \bar{f} \gamma_\mu (Q_f^{\text{G2HDM}} - a_f^\gamma \gamma_5) A^\mu f, \quad (14)$$

where

$$Q_f^{\text{G2HDM}} = \frac{\mathcal{O}_{1,1}^{4 \times 4}}{c_W} Q_f^{\text{SM}} + \frac{T_f^3}{2} \left(\frac{\mathcal{O}_{2,1}^{4 \times 4}}{s_W} - \frac{\mathcal{O}_{1,1}^{4 \times 4}}{c_W} \right) + \frac{1}{2e^{\text{SM}}} (g_X \mathcal{O}_{4,1}^{4 \times 4} X_R + g_H \mathcal{O}_{3,1}^{4 \times 4} T_{fR}^{3H}), \quad (15)$$

$$a_f^\gamma = \frac{T_f^3}{2} \left(\frac{\mathcal{O}_{2,1}^{4 \times 4}}{s_W} - \frac{\mathcal{O}_{1,1}^{4 \times 4}}{c_W} \right) - \frac{1}{2e^{\text{SM}}} (g_X X_R \mathcal{O}_{4,1}^{4 \times 4} + g_H T_{fR}^{3H} \mathcal{O}_{3,1}^{4 \times 4}). \quad (16)$$

Thus, with both nonzero M_X and M_Y , the electromagnetism interaction in G2HDM is in general different from the SM case. The standard charge assignment for every SM fermion will suffer from an overall correction factor of $\mathcal{O}_{1,1}^{4 \times 4}/c_W$ plus two correction terms, and there is also a non-vanishing axial vector coupling.

Next, we can take the limit $M_Y = 0$ and write the corresponding expressions. By replacing the elements of $\mathcal{O}^{4 \times 4}$ by $\mathcal{O}_{1,1}^{4 \times 4} = \mathcal{O}_{2,2}^{4 \times 4} = c_W$ and $-\mathcal{O}_{1,2}^{4 \times 4} = \mathcal{O}_{2,1}^{4 \times 4} = s_W$ as in Eq. (3), one can find the following new expressions for the vector and axial vector couplings

$$v_{f(M_Y=0)}^{(i)} = (T_f^3 - 2Q_f s_W^2) \mathcal{O}_{1i} + \frac{1}{\sqrt{g^2 + g'^2}} (X_R g_X \mathcal{O}_{3i} + T_{fR}^{3H} g_H \mathcal{O}_{2i}), \quad (17)$$

$$a_{f(M_Y=0)}^{(i)} = T_f^3 \mathcal{O}_{1i} - \frac{1}{\sqrt{g^2 + g'^2}} (X_R g_X \mathcal{O}_{3i} + T_{fR}^{3H} g_H \mathcal{O}_{2i}). \quad (18)$$

Similarly, one can do the same substitutions on Eqs. (15) and (16) together with $\mathcal{O}_{3,1}^{4 \times 4} = \mathcal{O}_{4,1}^{4 \times 4} = 0$ and check that the photon coupling to the SM fermions goes back to the SM expression $Q_f^{\text{G2HDM}} = Q_f^{\text{SM}} = T_f^3 + Y_f$ while all the axial vector couplings a_f^γ vanish. This is the main physical reason why we set $M_Y = 0$ so as to reproduce

the standard photon-fermion couplings. For M_X , it can be arbitrary and is naturally to consider the light and heavy scenarios where it is smaller and greater than the Z -boson mass respectively.

Obviously, the formulas obtained in this subsection for the couplings of the neutral gauge bosons with the SM fermions also hold for the heavy fermions in G2HDM.

III. THE CONSTRAINTS

A. Constraints from Precision Electroweak Data at LEP-I

The interaction of Z boson with SM fermions is described by the Lagrangian in Eq. (11). For the case of $M_Y = 0$ limit, the tree-level couplings are shown in Eqs. (17) and (18). For more precise calculation, we include the radiation corrections from propagator self-energies and flavor specific vertex corrections to the Z boson and fermions couplings [51, 52], which now are given by ² (suppressing $M_Y = 0$ in the subscripts)

$$v_f^i = \sqrt{\rho_f} (T_f^3 - 2\kappa_f Q_f s_W^2) \mathcal{O}_{1i} + \frac{1}{\sqrt{g^2 + g'^2}} (X_R g_X \mathcal{O}_{3i} + T_{fR}^{3H} g_H \mathcal{O}_{2i}) , \quad (19)$$

$$a_f^i = \sqrt{\rho_f} T_f^3 \mathcal{O}_{1i} - \frac{1}{\sqrt{g^2 + g'^2}} (X_R g_X \mathcal{O}_{3i} + T_{fR}^{3H} g_H \mathcal{O}_{2i}) , \quad (20)$$

where i in this work is either equal to 1 or 2 depending which mass eigenstate is closest to Z -pole. The parameters ρ_f and κ_f are loop corrections quantities. The decay of the Z boson into fermions and anti-fermions in the on-shell renormalization scheme is given by [51, 53]

$$\Gamma(Z \rightarrow f\bar{f}) = N_f^c \Gamma_o \mathcal{R}_f \sqrt{1 - 4\mu_f^2} \left[|v_f|^2 (1 + 2\mu_f^2) + |a_f|^2 (1 - 4\mu_f^2) \right] , \quad (21)$$

² We ignore loop corrections related to the new gauge couplings g_H and g_X .

where N_f^c is the color factor (1 for leptons and 3 for quarks), $\Gamma_o = G_F M_Z^3 / 6\sqrt{2}\pi$, $\mu_f = m_f/M_Z$ and

$$\mathcal{R}_f = \left(1 + \delta_f^{QED}\right) \left(1 + \frac{N_f^c - 1}{2} \delta_f^{QCD}\right), \quad (22)$$

with

$$\delta_f^{QED} = \frac{3\alpha}{4\pi} Q_f^2, \quad (23)$$

$$\delta_f^{QCD} = \frac{\alpha_s}{\pi} + 1.409 \left(\frac{\alpha_s}{\pi}\right)^2 - 12.77 \left(\frac{\alpha_s}{\pi}\right)^3 - Q_f^2 \frac{\alpha\alpha_s}{4\pi^2}. \quad (24)$$

Here Q_f is the electric charge of the fermion f in unit of e^{SM} , and α and α_s are the fine-structure and strong coupling constants, respectively, evaluated at the M_Z scale. It is understood that the couplings v_f and a_f in Eq. (21) should be replaced by v_f^i and a_f^i in Eqs. (19) and (20) respectively with $i = 1$ or 2 depending which M_{Z_i} is closest to the Z -pole M_Z .

We also investigate some Z -pole ($\sqrt{s} \approx M_Z$) observables, including the ratio of partial decay width of Z boson

$$R_l = \frac{\Gamma_{\text{had}}}{\Gamma_{l^+l^-}}, \quad R_q = \frac{\Gamma_{q\bar{q}}}{\Gamma_{\text{had}}}, \quad (25)$$

the hadronic cross-section

$$\sigma_{\text{had}} = \frac{12\pi\Gamma_{e^+e^-}\Gamma_{\text{had}}}{M_Z^2\Gamma_Z^2}, \quad (26)$$

the parity violation quantity

$$A_f = \frac{2v_f a_f}{v_f^2 + a_f^2}, \quad (27)$$

and the forward-backward asymmetry quantity

$$A_{\text{FB}} = \frac{3}{4} A_f \frac{A_e + P_e}{1 + P_e A_e}, \quad (28)$$

where P_e is the initial e^- polarization. Recall that at LEP-I $P_e = 0$, in this case

$$A_{\text{FB}}^{(0,f)} = \frac{3}{4} A_e A_f. \quad (29)$$

A summary of the electroweak observables at Z -pole from various experiments [43] is presented in Table II.

From the data in Table II, we build the Chi-squared for the electroweak observables at Z -pole as follows

$$\begin{aligned} \chi_{Z\text{-pole}}^2 = & \chi_{M_Z}^2 + \chi_{\sigma_{\text{had}}}^2 + \max \left[\chi_{\Gamma_Z}^2, (\chi_{\Gamma_{\text{had}}}^2 + \chi_{\Gamma_{\text{inv}}}^2 + \chi_{\Gamma_{l+l^-}}^2) \right] \\ & + \sum_{f=(e,\mu,\tau,b,c)} \chi_{R_f}^2 + \sum_{f=(e,\mu,\tau,b,c,s)} (\chi_{A_f}^2 + \chi_{A_{\text{FB}}^{(0,f)}}^2). \end{aligned} \quad (30)$$

Note that we have considered the correlations between the total decay width of Z boson and its partial decay widths to hadrons, invisibles and dilepton. For each χ_i^2 on the right-handed side of Eq. (30), it is given by the standard expression, namely

$$\chi_i^2 = \frac{(O_i^{\text{exp}} - O_i^{\text{th}})^2}{(\Delta O_i^{\text{exp}})^2}, \quad (31)$$

where $O_i^{\text{exp/th}}$ represents the experimental/theoretical value of any one of the 23 electroweak observables listed in Table II and ΔO_i^{exp} is the corresponding experimental uncertainty.

B. Contact Interactions at LEP-II

We also include constraints from data above the Z -pole by considering the LEP-II measurements related to contact interactions taking the following form of effective Lagrangian

$$\mathcal{L}_{\text{eff}} = \frac{\pm 4\pi}{(1 + \delta_{ef})(\Lambda_{\alpha\beta}^{\pm f})^2} (\bar{e}\gamma^\mu P_\alpha e \bar{f}\gamma_\mu P_\beta f), \quad (32)$$

where $P_{\alpha,\beta}$ represent the chirality projection operators with α, β being L or R for left-handed or right-handed fermions, respectively. The sign of Eq. (32) depends on whether the interference between the contact interaction it parametrizes and the SM process is constructive (+) or destructive (-). There is a total of 6 combinations

Observables	LEP Data	CEPC Precision [40]	Standard Model
M_Z [GeV]	91.1876 ± 0.0021	5×10^{-4}	91.1884 ± 0.0020
Γ_Z [GeV]	2.4952 ± 0.0023	5.06×10^{-4}	2.4942 ± 0.0008
Γ_{had} [GeV]	1.7444 ± 0.0020	—	1.7411 ± 0.0008
Γ_{inv} [MeV]	499.0 ± 1.5	—	501.44 ± 0.04
Γ_{l+l^-} [MeV]	83.984 ± 0.086	—	83.959 ± 0.008
σ_{had} [nb]	41.541 ± 0.037	—	41.481 ± 0.008
R_e	20.804 ± 0.050	—	20.737 ± 0.010
R_μ	20.785 ± 0.033	0.05%	20.737 ± 0.010
R_τ	20.764 ± 0.045	0.05%	20.782 ± 0.010
R_b	0.21629 ± 0.00066	0.08%	0.21582 ± 0.00002
R_c	0.1721 ± 0.0030	—	0.17221 ± 0.00003
$A_{\text{FB}}^{(0,e)}$	0.0145 ± 0.0025	—	0.01618 ± 0.00006
$A_{\text{FB}}^{(0,\mu)}$	0.0169 ± 0.0013	—	0.01618 ± 0.00006
$A_{\text{FB}}^{(0,\tau)}$	0.0188 ± 0.0017	—	0.01618 ± 0.00006
$A_{\text{FB}}^{(0,b)}$	0.0992 ± 0.0016	0.15%	0.1030 ± 0.0002
$A_{\text{FB}}^{(0,c)}$	0.0707 ± 0.0035	—	0.0735 ± 0.0001
$A_{\text{FB}}^{(0,s)}$	0.0976 ± 0.0114	—	0.1031 ± 0.0002
A_e	0.15138 ± 0.00216	—	0.1469 ± 0.0003
A_μ	0.142 ± 0.015	—	0.1469 ± 0.0003
A_τ	0.136 ± 0.015	—	0.1469 ± 0.0003
A_b	0.923 ± 0.020	—	0.9347
A_c	0.670 ± 0.027	—	0.6677 ± 0.0001
A_s	0.0895 ± 0.091	—	0.9356

TABLE II. The electroweak observables at the Z -pole. The second, third and last column are the LEP measurement [43], CEPC preliminary conceptual design report [40], and the SM prediction [43], respectively.

for the $\alpha\beta$ indices of $\Lambda_{\alpha\beta}^{\pm f}$: $\alpha\beta = \{LL, LR, RL, RR, VV, AA\}$, which are also called models. The limits on $\Lambda_{\alpha\beta}^{\pm f}$ set by LEP-II are given in Table 3.15 of Ref. [54]. The strongest constraint is given by $\Lambda_{VV}^{+l} > 24.6$ TeV. By using these $\Lambda_{\alpha\beta}^{\pm f}$ values, we are able to reconstruct the cross section for new physics processes based on the Lagrangian in Eq. (32).

To improve the analysis of this section, in particular for the cases where the mass of one of the gauge bosons is below the Z -pole, we calculate the additional Z -like mediator contribution³ to the $e^-e^+ \rightarrow Z_i \rightarrow f\bar{f}$ scattering cross section. In the case $f = e$ we have the contribution of both s and t channels while for $f \neq e$ only the s channel contributes. Note that here we do not need the SM contributions such as the photon and Z exchange not considered in Eq. (32). In the massless approximation for all the external fermions, the amplitudes for the s and t channels and for the interference term between them are given by:

$$|\mathcal{M}_s|^2 = \frac{2g_M^4 \{ [(a_f^i)^4 + (v_f^i)^4] (s^2 + 2st + 2t^2) - 2(a_f^i v_f^i)^2 (s^2 + 2st - 2t^2) \}}{(M_{Z_i}^2 - s)^2}, \quad (33)$$

$$|\mathcal{M}_t|^2 = \frac{2g_M^4 [(a_f^i)^4 (s^2 + t^2) - 2(a_f^i v_f^i)^2 (s^2 - 3t^2) + (v_f^i)^4 (s^2 + t^2)]}{(M_{Z_i}^2 + s + t)^2}, \quad (34)$$

$$|\mathcal{M}_{st}|^2 = \frac{4g_M^4 t^2 [(a_f^i)^4 + 6(a_f^i v_f^i)^2 + (v_f^i)^4]}{(M_{Z_i}^2 - s) (M_{Z_i}^2 + s + t)}, \quad (35)$$

where s is the center of mass energy squared, $t = s(\cos\varphi - 1)/2$ and φ is the angle between incoming and outgoing particles. This angle φ should be integrated to obtain the final cross section. The resulting cross section has to be compared against the cross section obtained using the effective Lagrangian in Eq. (32) with the $\Lambda_{\alpha\beta}^{\pm f}$ given by the experimental result. The couplings v_f^i and a_f^i have $i = 1$ or 2 depending on whether we are analyzing light or heavy M_X scenario. For $i = 3$, we assume

³ In what follows, we will denote the extra neutral gauge boson as Z' or Z_i depending on whether we refer to the experimental data or G2HDM.

M_{Z_3} is much heavier than M_Z so that its contributions are negligible. To be able to construct a χ^2 from the LEP-II 95% C.L. limit, we calculate the corresponding 95% C.L. cross section and compare against the theoretical result. When our theoretical result matches the 95% C.L. with null-signal assumption, the corresponding χ^2 value should be 2.71⁴. In this case, we calculate the χ^2 value using

$$\chi_{\text{LEP-II}}^2 = 2.71 \times \left[\frac{\sigma_{\text{G2HDM}}(e^+e^- \rightarrow Z_i \rightarrow f\bar{f})}{\overline{\sum \sigma_{\text{eff}}(\Lambda_{\alpha\beta}^{\pm f(95\%)})}} \right]^2, \quad (36)$$

where σ_{eff} is the cross section obtained using the effective Lagrangian of Eq. (32) with the experimental results for $\Lambda_{\alpha\beta}^{\pm f}$ given in Ref. [54] for different combinations of the chirality. The effective cross sections for different combinations of $\alpha\beta = \{LL, RR, LR, RL\}$ from the data are summed and averaged. We do not consider the combinations of VV and AA since they are not independent from the other polarizations considered above. Note that Eq. (36) goes to zero when the theoretical cross section vanishes (SM limit) as one would expect.

In the light M_X scenario (see Sec. IV C) in which one of the new neutral gauge boson is too light and invalidates the effective contact interaction approach, it is mandatory to recast the LEP-II constraints for the contact interactions into the cross section level to do the analysis. We checked that for the heavy M_X scenario, using either the effective contact interaction or cross section approach give the same results.

C. Drell-Yan Constraints at the LHC

In this section we recap the experiments of the Drell-Yan cross section for SM Z -boson and heavy Z' at the LHC.

⁴ For a Gaussian distribution, the value of $\Delta\chi^2 = 2.71$ corresponds to the 90% C.L. of a two-tailed test, but it also equivalent to the 95% C.L. of a one-tailed test that we are using.

1. *Z-boson on-shell decay at the LHC*

By using the measurement of the Drell-Yan cross section for the Z -boson production, the properties of the Z are well determined at the LHC. Among all the final states of the Z -boson decay, the dilepton signature is the most relevant to distinguish signal from background. It is commonly believed that the Drell-Yan constraint $q\bar{q} \rightarrow Z \rightarrow l^+l^-$ from the LHC is weaker than LEP EWPT data because of the relative larger uncertainties from the hadronic background than the QED background. However, to be careful, we first check a direct Drell-Yan constraints from the LHC [55]. The data of electron-positron pair (ee) and muon-pair ($\mu\mu$) final states are given by Tables 3 and 4 respectively in Ref. [55]. In the signal region located around Z -boson mass (the invariant mass $80 < m_{ll} / \text{GeV} < 120$), we found that the systematic uncertainties of Drell-Yan background is larger than the data statistic uncertainties in both ee or $\mu\mu$ final state. We have also checked that the EWPT constraints in Table II are much stronger than LHC Drell-Yan constraint.

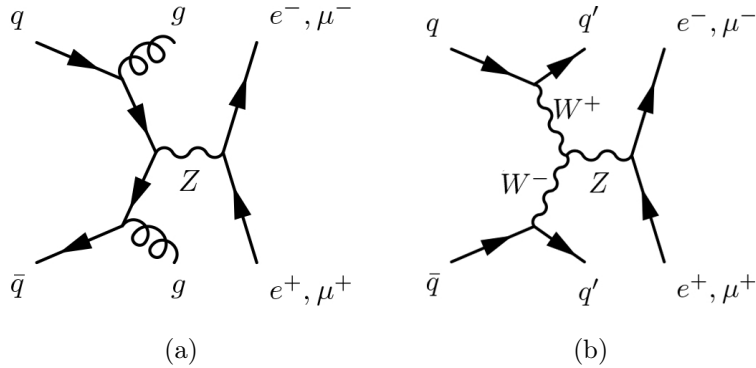


FIG. 1. The Feynman diagrams of electroweak Drell-Yan process.

On the other hand, Z -boson can be singly produced either by radiation from the incoming partons (Fig. 1a) or t -channel exchange of a W gauge boson (Fig. 1b). To constrain the G2HDM modified Zl^+l^- couplings, the later process is more use-

ful than the former because QCD processes usually suffer from larger systematical uncertainties than the electroweak ones. Recently, ATLAS [56] reported a fiducial electroweak cross section of $\sigma_{\text{EW}}^{Zjj} = 119 \pm 16 \pm 20 \pm 2$ fb and $\sigma_{\text{EW}}^{Zjj} = 34.2 \pm 5.8 \pm 5.5 \pm 0.7$ fb for dijet invariant masses m_{jj} greater than 250 GeV and 1 TeV, respectively. The SM simulated cross sections $\sigma_{\text{EW}}^{Zjj}(\text{SM})$ are also given in Table 5 of Ref. [56], where central values and the uncertainties are given as 125.2 ± 3.4 fb for $m_{jj} > 250$ GeV and 38.5 ± 1.5 fb for $m_{jj} > 1$ TeV.

Comparing with the SM, except for the Zl^+l^- couplings, the G2HDM did not modify much of the cross section. Namely, the electroweak cross section of the G2HDM version can be simply rescaled as

$$\sigma_{\text{EW}}^{Zjj}(\text{G2HDM}) = \sigma_{\text{EW}}^{Zjj}(\text{SM}) \times \mathcal{R}, \quad (37)$$

where

$$\mathcal{R} = \left[\frac{\mathcal{C}_{\text{G2HDM}}^{ZWW}}{\mathcal{C}_{\text{SM}}^{ZWW}} \right]^2 \frac{\text{BR}_{Z \rightarrow f\bar{f}}^{\text{G2HDM}}}{\text{BR}_{Z \rightarrow f\bar{f}}^{\text{SM}}} = \mathcal{O}_{11}^2 \frac{\text{BR}_{Z \rightarrow f\bar{f}}^{\text{G2HDM}}}{\text{BR}_{Z \rightarrow f\bar{f}}^{\text{SM}}}, \quad (38)$$

and $f = e, \mu$. However, similar to direct Drell-Yan Z boson search, we found that the value of \mathcal{R} is not easy to derivate from unity and the power of constraining the parameter space in G2HDM is not as strong as LEP EWPT constraints.

Finally, we have numerically verified that the allowed G2HDM parameter space is hardly changed at all whether the direct and electroweak Drell-Yan Z boson constraints at the LHC are included or not. Again, this is because both constraints at the LHC are much weaker than LEP EWPT constraints. Hence, we will not take into account the LHC Drell-Yan constraints from the on-shell Z decay in our numerical works so as to save some computer resources.

2. LHC Z' Boson Search at High-mass Dilepton Resonances

The Drell-Yan constraints can also be very powerful for the new gauge bosons in G2HDM once they can be singly produced [38]. Unlike the study in Ref. [38] which only W'^3 -like Z_i is considered, we extend it here to any Z_i with all the possible composition. Recently, ATLAS collaboration [57] reported a new result on dilepton resonances with the integrated luminosity of 139 fb^{-1} and the center-of-mass energy $\sqrt{s} = 13 \text{ TeV}$. They indicated that the lower limit on the mass of Z' boson for a simplified model can be raised up to $4 - 5 \text{ TeV}$. Considering this new measurement, we update the constraints of the heavy neutral gauge boson masses in G2HDM and the upper limits of g_H and g_X .

In Fig. 3 of Ref. [57], one can see the upper limits of cross section times branching ratio $\text{BR}(Z' \rightarrow l^+l^-)$ are based on the ratio of the total width $\Gamma_{Z'}$ of Z' divided by its $M_{Z'}$. Depending on this ratio, the limits can be altered by a factor of ~ 5 . As shown in Appendix B, the Γ_{Z_i}/M_{Z_i} in the G2HDM shall be always less than 0.06. Hence, for a conservative approach, we can simply apply the ATLAS result by using their upper limit associated with $\Gamma_{Z'}/M_{Z'} = 0.06$.

Furthermore, the Z_i total decay width relies on whether Z_i decays to the new particles in G2HDM. The heavy new fermions in G2HDM are assumed to be very heavy so that they do not affect the EW-scale physics in any significant way. On the other hand, the Z_i invisible decay to a scalar DM pair can be a more important channel because the upper limits of various parameters can be weaker than the one without taking into account the Z_i decays to the DM pair. The openings of the scalar channels as well as other channels with one vector and one scalar particles in the final states of Z_i decay makes the parameter spaces of the gauge and scalar sectors entangle with each other. Thus a complete analysis becomes quite formidable. In Eq. (B4), one can see that the invisible decay width of Z_i has two different limits,

$M_D \ll M_{Z_i}$ for maximum invisible decay and $M_D > M_{Z_i}$ for zero invisible decay. For the sake of simplicity, we will be contented by presenting the results based on these two benchmark invisible decay widths. In this study, we adopt $M_D = M_{Z_i}/10$ for maximum invisible decay but we found that the $\Gamma(Z_i \rightarrow DD^*)$ can differ within an accepted range of $\sim 6\%$ comparing with the massless M_D case.

Using `MadGraph5` [58], we compute the cross section $\sigma(pp \rightarrow Z_i)$. Since we enforce that the cross section is computed at the resonance, we only used a minimum cut given by the default parameter card in `MadGraph5`. It is very CPU time consuming to estimate the cross section point by point throughout all the parameter space. Nevertheless, the cross section can be obtained by simply rescaling the vector and axial vector couplings v_f^i and a_f^i using Eqs. (17) and (18). Hence, by using the same reasoning as before we include the latest ATLAS Z' limit in our scan by using the following chi-squared function

$$\chi_{\text{ATLAS}}^2 = 2.71 \times \left[\frac{\sigma_{\text{G2HDM}}(pp \rightarrow Z_i) \times \text{BR}_{\text{G2HDM}}(Z_i \rightarrow l^+l^-)}{\sigma_{\text{ATLAS}}^{95\%}(pp \rightarrow Z') \times \text{BR}_{\text{ATLAS}}^{95\%}(Z' \rightarrow l^+l^-)} \right]^2, \quad (39)$$

where the branching ratio $\text{BR}_{\text{G2HDM}}(Z_i \rightarrow l^+l^-)$ can be found in Appendix B and $\sigma_{\text{ATLAS}}^{95\%}(pp \rightarrow Z') \times \text{BR}_{\text{ATLAS}}^{95\%}(Z' \rightarrow l^+l^-)$ is 95% C.L. taken from the curve associated with $\Gamma_{Z'}/M_{Z'} = 0.06$ in Fig. 3 of Ref. [57].

IV. RESULTS

A. Numerical Methodology

Our aim is to determine the 68% and 95% allowed parameter space of the G2HDM which are favored by all of the experimental data presented in the previous section. In this paper, we will use the profile-likelihood (PL) method to perform the statistical data analysis. We recap the PL method in the following. Briefly, the PL method is a

well popular statistical method to deal with the multi-dimensional parameter space which treats the unwanted parameters as nuisance parameters. In other words, if a proposed model has n -dimensional parameter space and we are only interested in p of those dimensions, then the PL method can remove the unwanted $n - p$ dimensions which we are not interested in, by maximizing the likelihood over them.

There are 4 new parameters in the gauge sector of G2HDM. They are the two new gauge couplings g_H and g_X and the two new scales v_Φ and M_X . Our results will be presented in two-dimensional parameter regions with 68% and 95% confidence levels (C.L.). Take the plane (g_H, g_X) as an example. After marginalizing over the other two parameters v_Φ and M_X , an integral of the likelihood function $\mathcal{L}(g_H, g_X)$ can be written as

$$\frac{\int_{\mathcal{C}} \mathcal{L}(g_H, g_X) dg_H dg_X}{\text{normalization}} = \varrho, \quad (40)$$

where \mathcal{C} is the smallest area bound with a fraction ϱ of the total probability and the normalization in the denominator is the total probability with $\mathcal{C} \rightarrow \infty$.

The total $\chi_{\text{Total}}^2(g_H, g_X, v_\Phi, M_X)$ we will use in our analysis is the sum of Eqs. (30), (36), and (39), namely

$$\chi_{\text{Total}}^2 = \chi_{Z\text{-pole}}^2 + \chi_{\text{LEP-II}}^2 + \chi_{\text{ATLAS}}^2, \quad (41)$$

where we have suppressed the arguments of all the χ^2 functions. We adopt the statistical sensitivity as

$$\Delta\chi^2 = \chi_{\text{Total}}^2 - \min(\chi_{\text{Total}}^2). \quad (42)$$

Since our likelihood is modeled as a pure Gaussian distribution, *i.e.* $\mathcal{L} \propto \exp(-\chi^2/2)$, one can connect the χ^2 to the confidence level: the 68% (95%) C.L. in a two dimensional parameter space corresponding to $\Delta\chi^2 = -2 \ln(\mathcal{L}/\mathcal{L}_{\text{max}}) = 2.30$ (5.99). Here \mathcal{L}_{max} is the maximum value of the likelihood in the region \mathcal{C} .

There are two interesting scenarios: (i) heavy M_X and (ii) light M_X . The heavy M_X scenario will result in two new heavy neutral gauge bosons $Z_2 \equiv Z'$ and $Z_3 \equiv Z''$, and the measured boson located at Z -pole will be the lightest one, $Z_1 \equiv Z$. However, the light M_X scenario will result in a new boson Z_1 lighter than the Z -pole which is usually called dark Z (Z_D) or dark photon (γ_D). In this case, Z_2 corresponds to the Z -pole $Z_2 \equiv Z$ and $Z_3 \equiv Z'$. Hence, we choose our M_X scan ranges for two scenarios,

$$\frac{M_X}{\text{TeV}} : \begin{cases} [0.1 : 10] & (\text{heavy } M_X) \\ [10^{-6} : 0.08] & (\text{light } M_X) \end{cases} . \quad (43)$$

For the other three parameters, we use the same ranges for the two scenarios of M_X ⁵,

$$\begin{aligned} 10^{-8} \leq g_H \leq g^{\text{SM}} &= \frac{e^{\text{SM}}}{\sin \theta_W} = 0.65 , \\ 10^{-8} \leq g_X \leq g'^{\text{SM}} &= \frac{e^{\text{SM}}}{\cos \theta_W} = 0.35 , \\ 5 \text{ TeV} \leq v_\Phi &\leq 200 \text{ TeV} . \end{aligned} \quad (44)$$

We perform random scans by using MultiNest v2.17 [59] with 30000 living points, an enlargement factor reduction parameter 0.5 and a stop tolerance factor 10^{-3} . For sampling coverage, we combined several scans and finally obtained $\sim 10^5$ samples for each scenario.

B. Heavy M_X Scenario

In the heavy M_X scenario, the mass of Z_1 boson is located at around Z -pole (~ 91 GeV) so that Z_1 is identified as the SM Z -boson. Note that $Z_1(Z)$ boson physics is strongly affected by the different composition of Z_2 (Z') but not the heaviest boson

⁵ There is also the possibility of both M_X and v_Φ are light, which may lead to $Z_3 = Z$ and both Z_1 and Z_2 are lighter than Z . We will reserve this interesting scenario in future work.

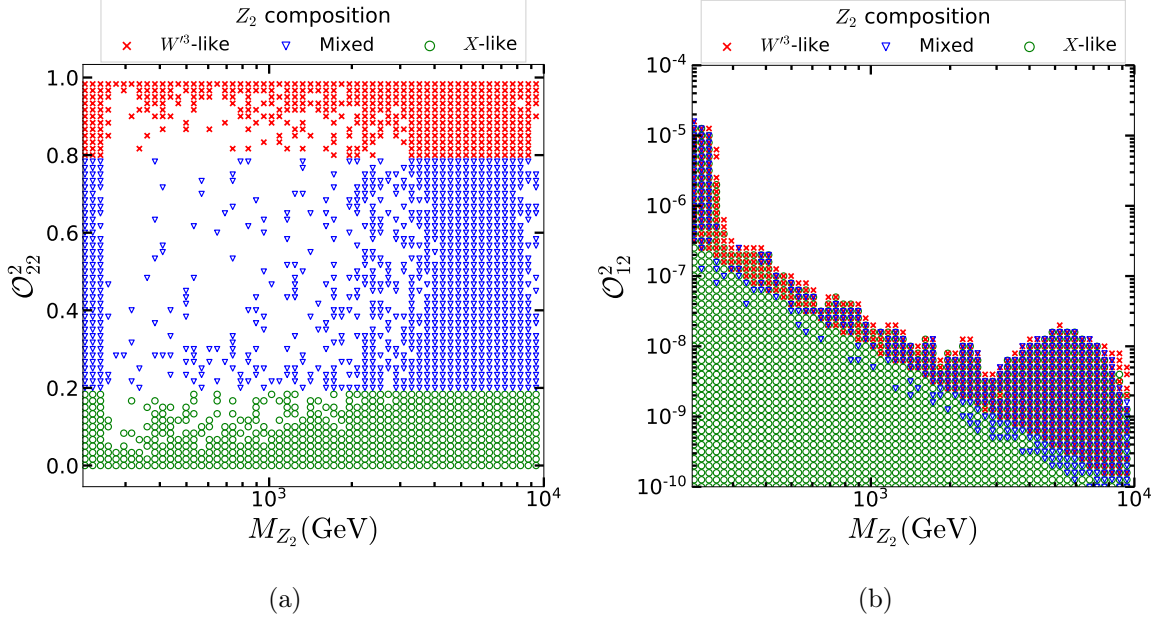


FIG. 2. Scatter plots in 1σ on (a) $(M_{Z_2}, \mathcal{O}_{22}^2)$ plane and (b) $(M_{Z_2}, \mathcal{O}_{12}^2)$ plane for the heavy M_X scenario. The red cross region with \mathcal{O}_{22}^2 between 0.8 and 1.0 represents the points of W'^3 -like Z_2 boson; the blue triangle region with \mathcal{O}_{22}^2 between 0.2 and 0.8 represents the points mixed with W'^3 , and the green circle region with \mathcal{O}_{22}^2 between 0.0 and 0.2 represents the points of X -like Z_2 boson.

Z_3 (Z'') because Z_3 is heavier than Z_2 in our parameter choices and therefore has less impact.

In Fig. 2, we present the scatter points of the composition of $Z_2 = \mathcal{O}_{12} Z^{\text{SM}} + \mathcal{O}_{22} W'^3 + \mathcal{O}_{32} X$ for the 1σ region based on the likelihoods described in Sec. IV A. The color code hereafter represents the three different composition of Z_2 . Recalling Eq. (10), we define W'^3 -like Z_2 with condition $\mathcal{O}_{22}^2 > 0.8$ (red crosses \times), mixed state Z_2 with $0.2 < \mathcal{O}_{22}^2 < 0.8$ (blue triangles ∇), and X -like Z_2 with condition $\mathcal{O}_{22}^2 < 0.2$ (green circles \circ).

The 1σ allowed scatter points projected on the (M_{Z_2}, O_{22}^2) and (M_{Z_2}, O_{12}^2) planes are depicted in Figs. 2a and 2b, respectively. From the density of distribution in Fig. 2a, we can clearly see that the mixed state Z_2 (blue triangles) is less evenly distributed because it needs some trade-off between the two new gauge couplings g_H and g_X . In Fig. 2b, we projected the same parameter space on the plane (M_{Z_2}, O_{12}^2) . Note that the mixing O_{12}^2 presents how Z_2 is consisted of Z^{SM} . Therefore, very small O_{12}^2 implies $O_{32}^2 \approx (1 - O_{22}^2)$ from the orthogonality of \mathcal{O} . Furthermore, the upper limit of v_Φ sets an lower limit of the O_{12}^2 for the red cross region. If v_Φ goes to infinity, Z_2 becomes super heavy and decouple. The composition of Z^{SM} in Z_2 should then be negligible, thus O_{12}^2 vanishes in this limit. We note that the excluded concave up region of M_{Z_2} between 250 GeV and 6 TeV on the upper limit of O_{12}^2 is due to the constraint from ATLAS Z' search.

In Fig. 3, we show the 1σ (dashed) and 2σ (solid) likelihood contours with scatter points inside the 1σ region on the (a) (M_{Z_2}, g_H) and (b) (M_{Z_2}, v_Φ) planes. In Fig. 3a, we can see that the W'^3 -like red crosses form a band with a tendency proportional to g_H . This is because for a W'^3 -like Z_2 , $m_{Z_2}^2 \approx g_H^2(v^2 + v_\Phi^2)/4 \approx g_H^2 v_\Phi^2/4$ which can be extracted from the (3,3) element of the mass matrix in Eq. (5). We can also see that at the lower bound of this band, the 95% and 68% C.L. contours are overlapped because this lower bound is due to our choice of $v_\Phi < 200$ TeV in its upper scan range, not from the likelihood results. This implies that in the upper edge of this red band where g_H has larger value, the value of v_Φ there is smaller. Therefore, the upper bound of this red cross band corresponds to the lower values of v_Φ , which can be excluded by the χ^2 tolerance as we can see in Fig. 3b where the scatter plot is projected on the (M_{Z_2}, v_Φ) plane. Surprisingly, in Fig. 3a, the blue triangle band, corresponding to mixing mostly between W'^3 and X bosons, matches the red cross band. This can be understood as the mass of Z_2 being dominated by the (3,3) element of Eq. (5) even for an 80% X boson composition. In the same figure, we can

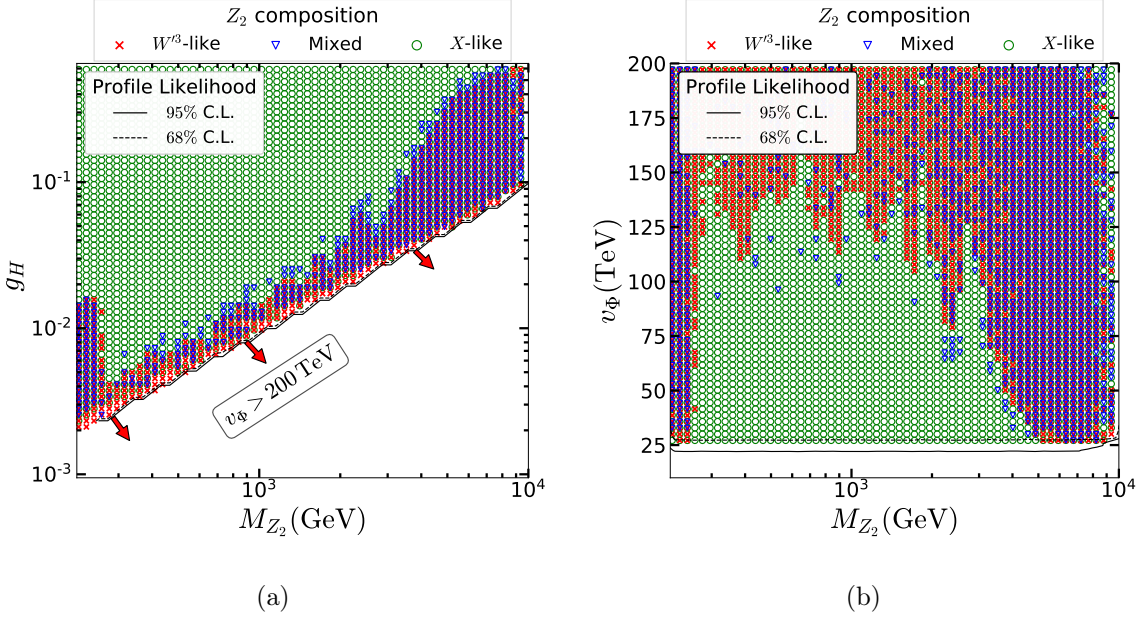


FIG. 3. Scatter plots in 1σ on (a) (M_{Z_2}, g_H) plane and (b) (M_{Z_2}, v_Φ) plane for the heavy M_X scenario. The color code is the same as Fig. 2. The 1σ and 2σ contours of the profile likelihood are also shown.

see the green circles running from below the two red cross and blue triangle bands up to the upper limit of g_H . In other words, we can see how the M_{Z_2} passes from being dominated by the (3,3) element of Eq. (5) (red crosses), which is g_H -dependent, to being dominated by the g_H -independent (4,4) element (green circles).

One particular feature of Fig. 3b is that the low M_{Z_2} and low v_Φ region (lower left corner) is covered only with X -like points while both W^{3} -like and mixed points only approach this corner down to a curved bound. This curved section in the lower bound can be related to the curved upper bound for W^{3} and mixed points in Fig. 3a for low $M_{Z_2} < 200$ GeV and $g_H \lesssim 10^{-2}$. These curves in the upper bound (Fig. 3a) and in the lower bound (Fig. 3b) can be understood as smaller v_Φ requiring larger g_H to pass EWPT. In particular, if g_H is small, v_Φ has to be large in order to have a

sizable diagonal (3,3) element in the mass matrix in Eq. (5), while the off-diagonal (2,3) and (3,2) elements remain small. However, the mixing effects from the off-diagonal elements are not negligible and expected to be stronger when the Z_2 mass is getting closer to the Z^{SM} mass. This gives rise to the upper and lower bounds that we see in Figs. 3a and 3b, respectively, for the W'^3 -like points. Such behaviour is not displayed for the X -like points since they do not depend strongly on g_H .

The ATLAS Z' constraint almost rules out the region $250 \text{ GeV} < M_{Z_2} < 6 \text{ TeV}$ for W'^3 -like and mixed Z_2 , except the region with $v_\Phi > 100 \text{ TeV}$. However, the X -like Z_2 at the same region has not been affected much by the ATLAS Z' constraint.

Similarly, in Fig. 4, we show the 1σ (dashed) and 2σ (solid) likelihood contours with scatter points inside the 1σ region on the (a) (M_{Z_3}, g_H) and (b) (M_{Z_3}, g_X) planes. From Fig. 4a, one can easily see that the X -like Z_2 boson (green circles) forms a band whose tendency is proportional to the g_H . This can be understood by the fact that the composition of the Z_3 in this case is mainly from W'^3 , which has a mass proportional to $0.5 g_H \sqrt{v^2 + v_\Phi^2} \approx 0.5 g_H v_\Phi$ again coming from the (3,3) element of the mass matrix in Eq. (5). On the other hand, in the case of the W'^3 -like Z_2 boson (red crosses), the mass of the Z_3 almost does not depend on g_H . Indeed, the composition of Z_3 is now mainly from X and $M_{Z_3}^2 \approx (g_X^2(v^2 + v_\Phi^2) + M_X^2)$. This is clearly shown in Fig. 4b, when g_X is small ($g_X < 3 \times 10^{-3}$), the mass of Z_3 in the red cross region is dominated by M_X and less than our set-up limit of 10^4 GeV . However, when g_X is getting bigger, the mass of the Z_3 can be dominated by the $g_X v_\Phi$ term for sufficiently large value of v_Φ . We can also see that the EWPT data sets upper bounds on g_H and g_X . The excluded concave up region of $250 \text{ GeV} < M_{Z_2} < 6 \text{ TeV}$ in Fig. 4a for the W'^3 -like and mixed composition of Z_2 is again due to the ATLAS Z' search which does not apply for the X -like case. As a result, the ATLAS Z' search cannot constrain on g_X for W'^3 -like points as clearly shown in Fig. 4b.

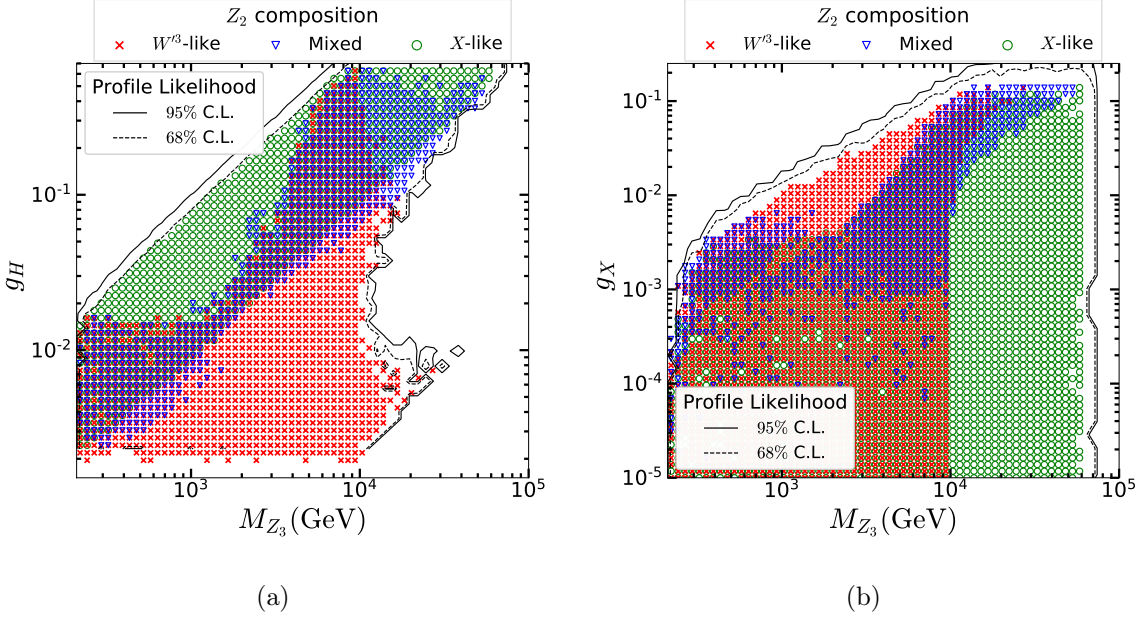


FIG. 4. Scatter plots in 1σ on (a) (M_{Z_3}, g_H) plane and (b) (M_{Z_3}, g_X) plane for the heavy M_X scenario. The color code is the same as Fig. 2. The 1σ and 2σ contours of the profile likelihood are also shown.

C. Light M_X Scenario

In the light M_X scenario, we require that the mass of Z_2 boson is always at around Z -pole (~ 91 GeV). In this scenario, the lightest Z_1 with mass less than the Z -boson mass can be the dark photon or dark Z , while the conventional Z' is the heaviest boson Z_3 . We note that the composition of Z_3 is given by $Z_3 = \mathcal{O}_{13}Z^{\text{SM}} + \mathcal{O}_{23}W'^3 + \mathcal{O}_{33}X$. The 1σ allowed scatter points projected on the (M_{Z_3}, O_{23}^2) and (M_{Z_3}, O_{13}^2) planes are depicted in Figs. 5a and 5b, respectively. The color code for the composition of Z_3 is the same as in Fig. 2 for Z_2 .

An obvious feature of Fig. 5a is that the mixed state of Z_3 (blue triangles) has a mass upper limit. Intuitively, it requires some trade-off between the gauge couplings

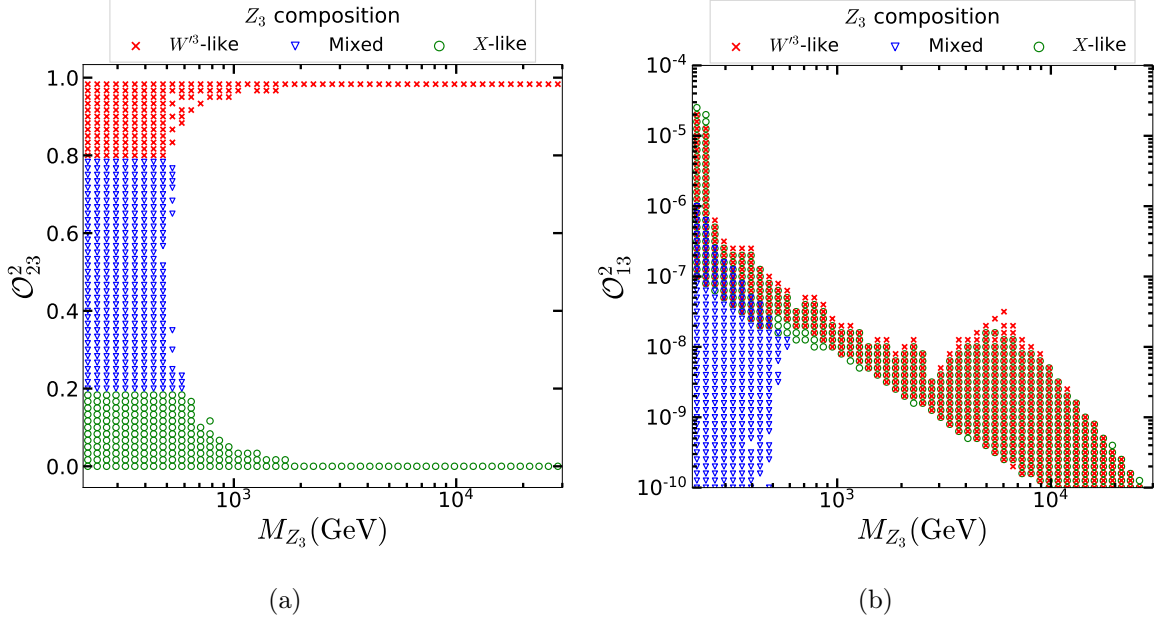


FIG. 5. Scatter plots in 1σ region on (a) (M_{Z_3}, O_{23}^2) plane and (b) (M_{Z_3}, O_{13}^2) plane for the light M_X scenario. The red cross represents the points of W'^3 -like Z_3 boson, the blue triangle represents the points mixed states (Z^{SM} , W'^3 and X) Z_3 boson, and the green circles represents X -like Z_3 boson.

g_H and g_X which results in $M_{Z_3} \lesssim 500$ GeV. This effect will be discussed with more detail later in Fig. 6. In Fig. 5b, we can see that the Z^{SM} composition of Z_3 is again small. However, unlike the heavy M_X scenario, the X -like Z_3 boson has a similar distribution as W'^3 -like Z_3 boson. Additionally, the mixed Z_3 state at the mass region between 210 GeV and 700 GeV cannot be excluded by the ATLAS Z' constraint which is also different from the heavy M_X scenario.

In analogous to Fig. 3, we show in Fig. 6 the 1σ (dashed) and 2σ (solid) likelihood contours with scatter points in the 1σ region on the (a) (M_{Z_3}, g_H) and (b) (M_{Z_3}, v_Φ) planes. Comparing Figs. 3a and 6a, we have a clear separation between the W'^3 -

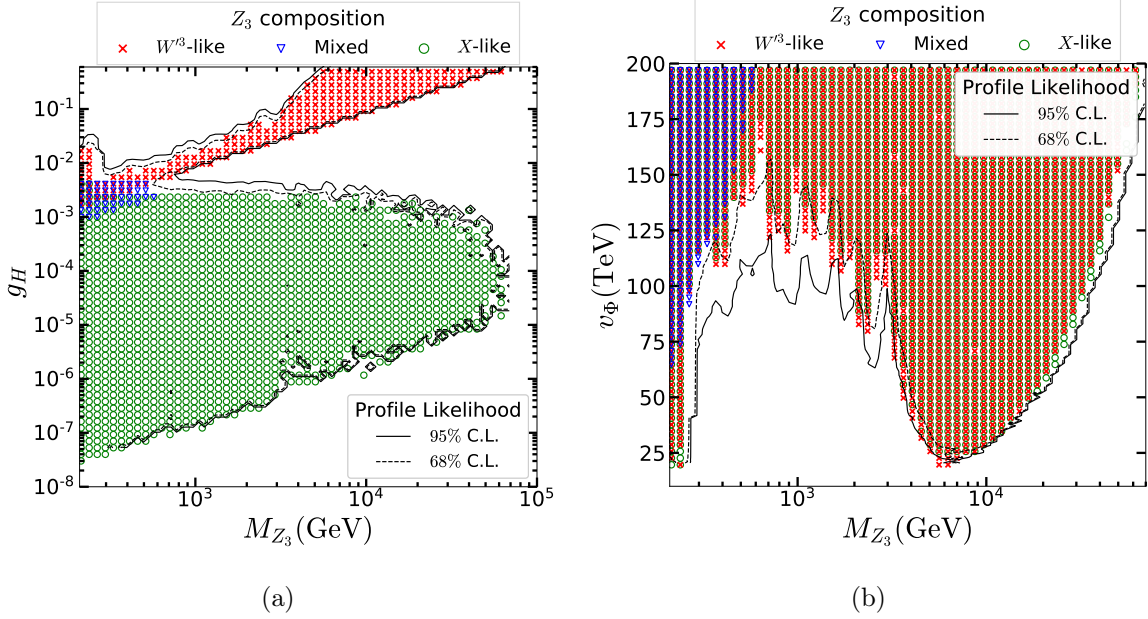


FIG. 6. Scatter plots in 1σ on (a) (g_H, M_{Z_3}) plane and (b) (v_Φ, M_{Z_3}) plane for the light M_X scenario. The markers are the same as Fig. 5. The 1σ and 2σ contours of the profile likelihood are also shown.

like (red crosses) and X -like (green circles) regions in this light M_X scenario. As before, the W'^3 -like red crosses follow a tendency proportional to g_H again because of the dominance of the $(3,3)$ element of Eq. (5) in M_{Z_3} , *i.e.*, $M_{Z_3} \approx g_H v_\Phi / 2$. Other features shared between W'^3 -like points in Figs. 3a and 6a are the distribution of v_Φ values; the g_H lower bound owes to v_Φ upper bound but its upper bound owes to χ^2 tolerance. As expected, the ATLAS Z' search can constrain g_H and v_Φ at the mass region $250 \text{ GeV} < M_{Z_2} < 6 \text{ TeV}$. However, the gauge coupling for X -like Z_3 is proportional to g_X not g_H so that the ATLAS Z' search cannot constrain on g_H at the X -like region, indicated by green circles. The X -like region in Fig. 6a has a g_H upper bound around 10^{-2} given by the χ^2 tolerance and most likely related to the lower bound on v_Φ displayed on Fig. 6b. The mass of Z_3 , M_{Z_3} , in this X -like

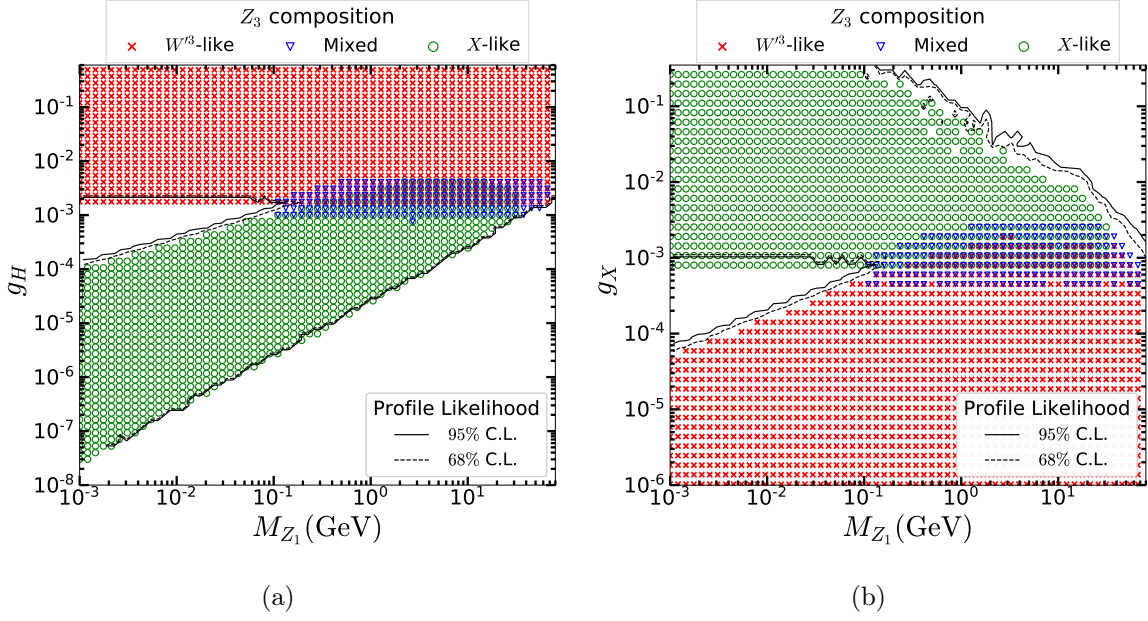


FIG. 7. Scatter plots in 1σ on (a) (g_H, M_{Z_1}) plane and (b) (g_X, M_{Z_1}) plane for the light M_X scenario. The markers are the same as Fig. 5. The 1σ and 2σ contours of the profile likelihood are also shown.

green region can be approximated by $\sqrt{g_X^2 v_\Phi^2 + M_X^2}$, this is why there is not a clear g_H dependence as in the W^3 -like points. In Fig. 6a, as one would expect, the mixed region corresponds approximately to the intersection between X -like and W^3 -like regions, extending lightly into their exclusive regions. This means that the upper and lower bound of the mixed region are approximately given by the upper bound of the X -like region and the lower bound of the W^3 -region, respectively. If we increase our maximum v_Φ value, the lower bound of the W^3 -like region would reach lower g_H and the maximum M_{Z_3} for the mixed region would be increased. This is more clear after looking at Fig. 6b where the maximum M_{Z_3} value for the three regions grows with the value of v_Φ .

Similarly, in Fig. 7, we show the 1σ (dashed) and 2σ (solid) likelihood contours

with scatter points in the 1σ region on the (a) (M_{Z_1}, g_H) plane and (b) (M_{Z_1}, g_X) planes. Again, the red cross represents the points of W'^3 -like Z_3 boson, the blue triangle represents the points of mixed state (Z^{SM}, W'^3 and X) Z_3 boson, and the green circle represents X -like Z_3 boson. We note that in this scenario, Z_1 is considered as a dark photon ⁶ and has mass range from 1 MeV to Z -pole. One can easily see that the Z_3 composition is clearly separated on the planes of (M_{Z_1}, g_H) and (M_{Z_1}, g_X) . In particular, while the W'^3 -like Z_3 boson parameter space is distributed in the region of larger g_H and smaller g_X , the X -like Z_3 boson, in contrast, prefers to be in the region of smaller g_H and larger g_X . The mixed composition of Z_3 lies in the range of $7 \times 10^{-4} < g_H < 5 \times 10^{-3}$ and $4 \times 10^{-4} < g_X < 3 \times 10^{-3}$. For the X -like Z_3 boson region in Fig. 7a, there is a lower bound for g_H due to our choice of 200 TeV as the upper bound for v_Φ . Moreover, in Fig. 7b, one can also see that the χ^2 tolerance sets an upper limit on g_X as the Z_1 boson mass gets heavier.

Finally, we would like to emphasize that the contact interaction exclusion regions at $M_{Z_1} < 200$ MeV and $10^{-4} < g_X, g_H < 10^{-3}$ are owing to two different coupling components, $g_H \mathcal{O}_{2i}$ and $g_X \mathcal{O}_{3i}$ in Eqs. (17) and (18).

D. Future Prospects

Since current LEP together with other constraints already put a severe limit on the parameter space, it will be interesting to see whether the future Z -boson precision experiments can further probe our model. In the near future, there are three colliders that can improve Z -boson measurements: CEPC [40], ILC [60], and FCC-ee [61]. Among them, CEPC is the one that could give the most sensitive limit. Therefore, in this subsection, we make an estimation of our parameter space with

⁶ The lightest boson Z_1 can be tested in the dark photon experiments but it is beyond the scope of this work. We will return to this in the future.

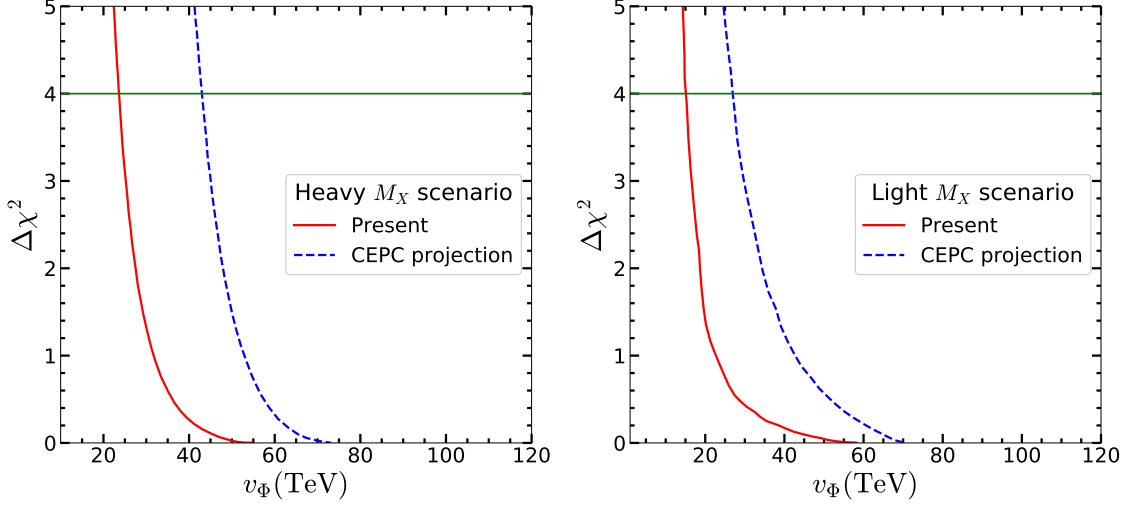


FIG. 8. The $\Delta\chi^2$ as function of v_Φ . The red solid line and blue dashed line are based on present constraint and future CEPC sensitivity. The left and right panels are corresponding to heavy and light M_X scenarios, respectively.

the projected CEPC sensitivity.

In the third column of Table II, we quote the expected CEPC sensitivity [40]. Apparently, some of the error bars are expected to be significantly reduced. Note that the CEPC preliminary conceptual design report does not provide a full list as the LEP measurements showed in the 2nd column. Therefore, for those missing rows, we reuse the data from the 2nd column (LEP data).

To start with, we present the $\Delta\chi^2$ in terms of v_Φ in Fig. 8 for heavy (left) and light (right) M_X scenarios. Importantly, v_Φ is the most sensitive parameter in the G2HDM, determining the theory scale. For the heavy M_X scenario, in the present sensitivity case the 2σ lower bound is around 24 TeV, while in the CEPC case it is around 44 TeV. For the light M_X scenario, the 2σ current and CEPC lower limit of v_Φ is smaller than the heavier M_X scenario. In particular, $v_\Phi > 15$ TeV (36 TeV) at 95% C.L. from current experiments (CEPC). The difference between these two

scenarios is owing to the different sources of constraints on v_Φ . For the heavy M_X scenario, the EWPT constraints of the SM Z boson play an important role in raising the lower limit of v_Φ . However, for the light M_X scenario, the main constraint to exclude the lower v_Φ region is from Z' searches. This also explains why the future sensitivity does not further push v_Φ in the light M_X scenario to larger values as the heavy M_X scenario does because the future sensitivities of contact interactions are not available for CEPC and only the previous limits from LEP II are used.

In Fig. 9, we compare the present limit and future CEPC sensitivity of the two-dimensional contours on the (g_H, g_X) plane. The figure in the left (right) column corresponds to the heavy (light) M_X scenario. Because the upper scan limit of g_H is set to be less than g_2^{SM} , the experimental constraints on g_H are not present. In contrast, g_X has an upper limit from the constraints due to g_H having a lower limit from the maximum scanned v_Φ value. The upper limit of g_H can be further improved by future CEPC sensitivity along the edge of the contour. However, the light M_X scenario is mildly constrained by future CEPC sensitivity. The two contour plots in Fig. 9 can be further understood as follows. We note that, for the case of W'^3 -like Z_2 in heavy M_X scenario (left panel) or W'^3 -like Z_3 in light M_X scenario (right panel), g_H has a lower limit at $\sim 2 \times 10^{-3}$ due to our choices of the parameter scan ranges. Indeed, in both cases we have $M_{Z_{2,3}} \approx 0.5g_H\sqrt{v^2 + v_\Phi^2}$ which implies that $g_H \approx (2M_{Z_{2,3}})/\sqrt{v^2 + v_\Phi^2}$. Since we require $M_{Z_{2,3}} > 210$ GeV and $v_\Phi < 200$ TeV, this implies $g_H > 2 \times 10^{-3}$. Similarly, for the case of X -like Z_3 in the light M_X scenario (upper right panel), the mass of Z_3 , is given by $M_{Z_3} \approx \sqrt{g_X^2(v^2 + v_\Phi^2) + M_X^2}$ so that we can obtain $g_X \approx \sqrt{M_{Z_3}^2 - M_X^2}/\sqrt{v^2 + v_\Phi^2}$. This yields a lower limit for g_X at $\sim 10^{-3}$ when we require $M_{Z_3} > 210$ GeV, $M_X < 80$ GeV and $v_\Phi < 200$ TeV. On the other hand, g_X has no lower limit in the heavy M_X scenario (left panel).

The Stüeckelberg mass parameter M_X is a filter to split the parameter space into two scenarios but we have not been able to constrain this parameter. The reason

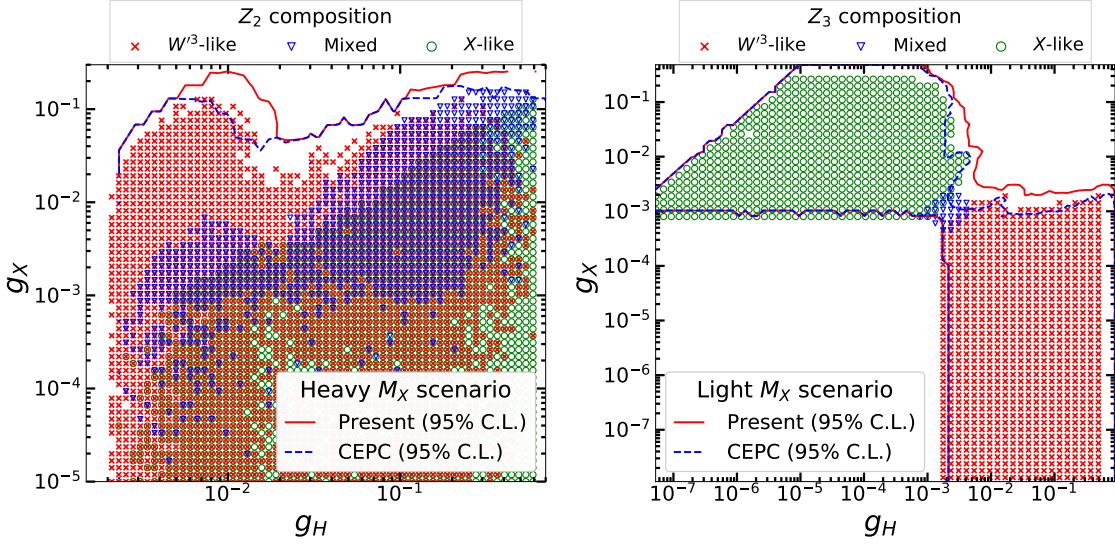


FIG. 9. The present and future sensitivity allowed regions projected on the (g_H, g_X) plane in both heavy (left) and light (right) M_X scenarios. The red solid line is for the present 95% limit while the blue dashed line is for the CEPC future sensitivity. Scatter points in 1σ region of the present constraint are also shown. The color codes in the left and right panel are same as in Figs. 2 and Fig. 5, respectively.

is simply that Z_3 in the heavy M_X scenario is too heavy to be relevant by current experiments. On the other hand, in the light M_X scenario with $M_X < 80$ GeV, it is again too light to be presented in the EWPT data. To constrain light M_X , just like dark photon, the lightest Z_1 could be detected by those future beam dump experiments such as NA62 [62], Belle II [63], and SHiP [64]. However, this is beyond the scope of this work and we will return to it in the future.

V. SUMMARY AND CONCLUSION

In this paper, we perform an updated profile likelihood analysis for the gauge sector of G2HDM.

For the two Stüeckelberg mass parameters M_Y and M_X associated with the hypercharge $U(1)_Y$ and the extra $U(1)_X$ respectively, we showed that a nonzero M_Y would produce non-standard QED couplings for all the fermions in G2HDM, albeit we can always achieve a massless photon for arbitrary values of M_X and M_Y . We therefore set $M_Y = 0$ in our numerical analysis. The remaining new parameters in the gauge sector of G2HDM needed to be constrained are g_H , g_X , v_Φ and M_X .

We have examined the remaining parameter space with the EWPT LEP data at the Z -pole, contact interaction constraints from LEP-II and LHC Run II data for the search of high-mass dilepton resonances. The contact interactions constraints can definitely provide a lower limit on v_Φ , but the EWPT data play a significant role to constrain the parameter space non-trivially. While the LHC search for the high-mass dilepton resonances also impose important constraints on the parameter space, the Drell-Yan data from the Z decay does not impose noticeable impacts yet.

We classify our parameter space based on three different composition (X -like, W'^3 -like, and mixed) of the heavy neutral gauge boson, either Z_2 or Z_3 , which is the next-heavier Z boson than the SM one, in order to manifest the physics and constraints discussed in this paper.

In the heavy M_X scenario ($M_X > 100$ GeV), the SM-like Z is the lightest Z_1 boson and EWPT constraints exclude the small v_Φ region up to 24 TeV at 2σ significance. However, the EWPT constraints are not so sensitive to the light M_X scenario ($M_X < 80$ GeV) where SM-like Z is the next-lightest Z_2 boson. In particular, the v_Φ is required to be greater than 15 TeV due to the constraints of Z' contact interaction search from LEP-II and high-mass dilepton resonance search from LHC Run II.

Furthermore, in both light and heavy M_X scenarios, M_X is just a parameter to tweak between two scenarios and it is totally unbounded in this study. It is likely that the future dark photon searches might set a limit on the M_X in the light M_X scenario. On the other hand, it is not so trivial for the couplings g_X and g_H because we found it is hard to set an upper bound on them individually.

Although the SM Z boson is fixed at the Z -pole, the allowed physical masses of the heavier Z_i still depend on the M_X and detailed composition. Generally speaking, the Z_2 allowed mass range in the heavy M_X scenario is same as the range of M_X but Z_3 mass can reach up to 70 TeV for X -like composition and 40 TeV for both W'^3 -like and mixed composition. Like the role of M_X in the heavy scenario, the M_{Z_1} in the light M_X scenario is dominated by M_X and the allowed mass ranges of M_{Z_1} have no difference between different composition. However, regarding to M_{Z_3} , mixed Z_3 is restricted to less than 500 GeV but the masses of X -like and W'^3 -like Z_3 are below 70 TeV.

Finally, we also discuss the future sensitivity of the new parameters at the CEPC. We found that the CEPC can significantly probe the parameter space of the heavy M_X scenario but the sensitivity is not improved much for the light M_X scenario. In the latter case, when M_X is getting very light, Z_1 can be much lighter than the Z -boson and it is more appropriate to identify it as the dark photon or dark Z_D . The very rich phenomenology of light dark photon or dark Z_D in G2HDM remains to be explored in the future.

ACKNOWLEDGMENTS

We would like to thank Wei-Chih Huang, Zuowei Liu and Xun Xue for stimulating discussions. This work was supported in part by the Ministry of Science and Technology (MoST) of Taiwan under Grant Nos. 107-2119-M-001-033- and 107-2811-M-001-027-. Y.-L. S. Tsai was funded in part by Chinese Academy of Sciences Taiwan Young Talent Programme under Grant No. 2018TW2JA0005. V. Q. Tran was funded in part by the National Natural Science Foundation of China under Grant Nos. 11775109, U1738134 and by the National Recruitment Program for Young Professionals.

Appendix A: The Rotation Angles ϕ , θ and ψ

In this appendix, we will show how to obtain the equations of the rotation angles such as Eqs. (7), (8) and (9) from the orthogonal matrix which diagonalizes the mass matrix $\mathcal{M}_{\text{gauge}}^2(M_Y = 0)$ given in Eq. (5). The orthogonal matrix we choose is Eq. (6) because it is rather convenient to find all the \mathcal{O}_{ij} s and determine the rotational angles ϕ , θ and ψ numerically. However, the computation of the angles in terms of the fundamental parameters in the Lagrangian are difficult to organize into nice forms using Eq. (6) for \mathcal{O} , so we apply Cramer's rule for solving the secular equations and get another form for \mathcal{O} as follows

$$\mathcal{O} = \begin{pmatrix} |x_1|/\Delta_1 & x_2/\Delta_2 & x_3/\Delta_3 \\ y_1/\Delta_1 & |y_2|/\Delta_2 & y_3/\Delta_3 \\ z_1/\Delta_1 & z_2/\Delta_2 & |z_3|/\Delta_3 \end{pmatrix}, \quad (\text{A1})$$

where

$$\Delta_i = \sqrt{x_i^2 + y_i^2 + z_i^2}, \quad (\text{A2})$$

and

$$\begin{aligned}
x_1 &= \begin{vmatrix} M_{22}^2 - M_{Z_1}^2 & M_{23}^2 \\ M_{32}^2 & M_{33}^2 - M_{Z_1}^2 \end{vmatrix}, \quad y_1 = s_{x_1} \begin{vmatrix} M_{23}^2 & M_{21}^2 \\ M_{33}^2 - M_{Z_1}^2 & M_{31}^2 \end{vmatrix}, \quad z_1 = s_{x_1} \begin{vmatrix} M_{21}^2 & M_{22}^2 - M_{Z_1}^2 \\ M_{31}^2 & M_{32}^2 \end{vmatrix}, \\
x_2 &= s_{y_2} \begin{vmatrix} M_{13}^2 & M_{12}^2 \\ M_{33}^2 - M_{Z_2}^2 & M_{32}^2 \end{vmatrix}, \quad y_2 = \begin{vmatrix} M_{11}^2 - M_{Z_2}^2 & M_{13}^2 \\ M_{31}^2 & M_{33}^2 - M_{Z_2}^2 \end{vmatrix}, \quad z_2 = s_{y_2} \begin{vmatrix} M_{12}^2 & M_{11}^2 - M_{Z_2}^2 \\ M_{32}^2 & M_{31}^2 \end{vmatrix}, \\
x_3 &= s_{z_3} \begin{vmatrix} M_{12}^2 & M_{13}^2 \\ M_{22}^2 - M_{Z_3}^2 & M_{23}^2 \end{vmatrix}, \quad y_3 = s_{z_3} \begin{vmatrix} M_{13}^2 & M_{11}^2 - M_{Z_3}^2 \\ M_{23}^2 & M_{21}^2 \end{vmatrix}, \quad z_3 = \begin{vmatrix} M_{11}^2 - M_{Z_3}^2 & M_{12}^2 \\ M_{21}^2 & M_{22}^2 - M_{Z_3}^2 \end{vmatrix},
\end{aligned} \tag{A3}$$

with M_{ij}^2 stands for the element of $\mathcal{M}_{\text{gauge}}^2(M_Y = 0)$, $M_{Z_i}^2 (i = 1, 2, 3)$ are the mass eigenvalues and $s_{x_i} = \text{sign}(x_i)$. From Eq. (6), one can obtain the following relations for the rotational angles ϕ , θ and ψ ⁷

$$\phi = \arctan\left(\frac{-\mathcal{O}_{12}}{\mathcal{O}_{22}}\right), \quad \theta = \arctan\left(\frac{-\mathcal{O}_{32}}{\mathcal{O}_{12}} \sin \phi\right), \quad \psi = \text{arccot}\left(\frac{-\mathcal{O}_{21} \cos \theta}{\mathcal{O}_{31} \sin \phi} - \sin \theta \cot \phi\right), \tag{A4}$$

with the range for θ covers π radians, and the range for ϕ and ψ covers 2π radians. Note that the expressions in Eq. (A4) do not depend on the Δ_i given in Eq. (A2). Using Eqs. (A1) and (A3) for the various \mathcal{O}_{ij} in Eq. (A4), after some algebra, one can obtain Eqs. (7), (8) and (9), which are collected here again for convenience.

$$\tan(\phi) = \frac{-g_H v M_{Z\text{SM}} (M_X^2 - M_{Z_2}^2 + 2g_X^2 v_\Phi^2)}{2\left(M_{Z_2}^4 - (M_{Z\text{SM}}^2 + M_X^2 + (v^2 + v_\Phi^2)g_X^2)M_{Z_2}^2 + M_{Z\text{SM}}^2(M_X^2 + g_X^2 v_\Phi^2)\right)}, \tag{A5}$$

$$\tan(\theta) = \frac{-g_X (M_{Z_2}^2 (v^2 - v_\Phi^2) + M_{Z\text{SM}}^2 v_\Phi^2)}{v M_{Z\text{SM}} (M_X^2 - M_{Z_2}^2 + 2g_X^2 v_\Phi^2)} \sin \phi, \tag{A6}$$

$$\cot(\psi) = \frac{g_H (M_{Z_1}^2 - M_X^2 - 2g_X^2 v_\Phi^2) \cos \theta}{g_X (g_H^2 v_\Phi^2 - 2M_{Z_1}^2)} \sin \phi - \sin \theta \cot \phi. \tag{A7}$$

⁷ We note that similar approach had been used in [65] for the scalar boson mass matrix in MSSM with explicit CP violation.

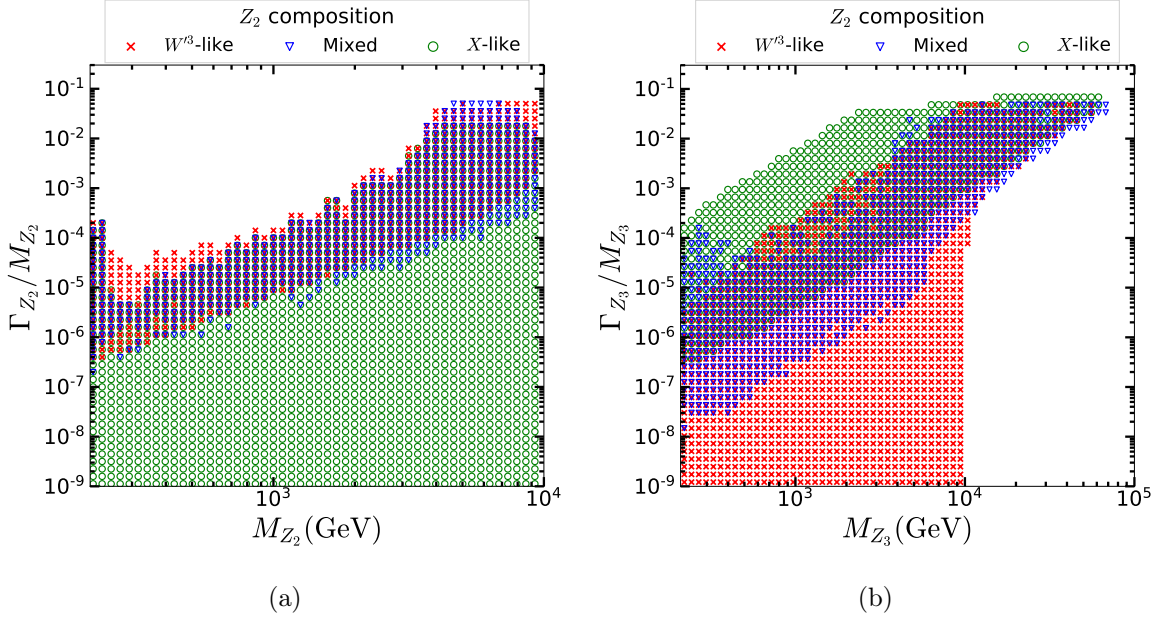


FIG. 10. Heavy M_X scenario: scatter plots in 1σ region on the (a) $(\Gamma_{Z_2}/M_{Z_2}, M_{Z_2})$ and (b) $(\Gamma_{Z_3}/M_{Z_3}, M_{Z_3})$ planes. The markers are the same as Fig. 2.

Thus one can compute the rotation angles in terms of the fundamental parameters of the model which can provide some useful insights in the vanishing limits of g_H and g_X as discussed in Section (II B).

Appendix B: Decay Widths of New Neutral Gauge Bosons

In this appendix, we show the decay widths of the two new neutral gauge bosons Z_i . We note that for light M_X scenario, $i = (1, 3)$, while for heavy M_X scenario, $i = (2, 3)$.

- The decay width of Z_i to a pair of fermions (including both SM and new heavy

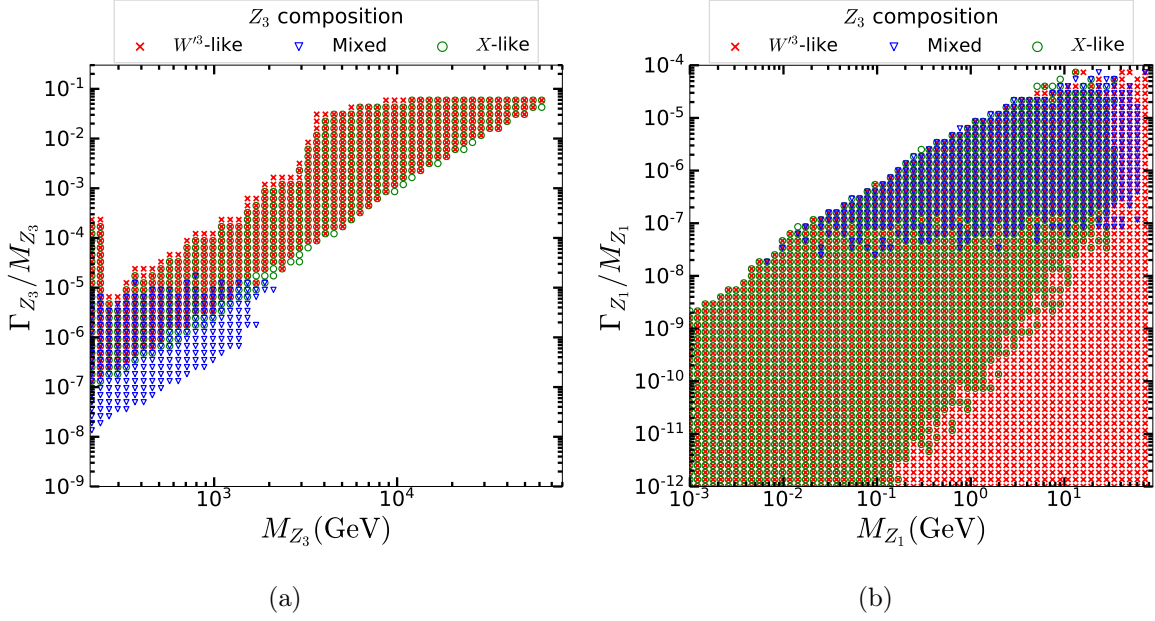


FIG. 11. Light M_X scenario: scatter plots in 1σ on the (a) $(\Gamma_{Z_3}/M_{Z_3}, M_{Z_3})$ and (b) $(\Gamma_{Z_1}/M_{Z_1}, M_{Z_1})$ planes. The markers are the same as Fig. 5.

fermions) is given as follows

$$\Gamma(Z_i \rightarrow f\bar{f}) = \frac{N_f^c g_M^2 M_{Z_i}}{12\pi} \sqrt{1 - 4r_{if}} \left((2r_{if} + 1)|v_f^{(i)}|^2 + (1 - 4r_{if})|a_f^{(i)}|^2 \right), \quad (\text{B1})$$

where $g_M = \sqrt{g^2 + g'^2}/2$, N_f^c is the number of color for fermion f , the coefficients $v_f^{(i)}$ and $a_f^{(i)}$ are the couplings that appear in Eqs. (17) and (18) and $r_{if} = \frac{m_f^2}{M_{Z_i}^2}$.

- The decay width for $Z_i \rightarrow W^+W^-$ process is given by [66]

$$\Gamma(Z_i \rightarrow W^+W^-) = \frac{g_{Z_i WW}^2 M_{Z_i}}{192\pi r_{iW}^2} (1 - 4r_{iW})^{3/2} \left(1 + 20r_{iW} + 12r_{iW}^2 \right), \quad (\text{B2})$$

where $r_{iW} = \frac{M_W^2}{M_{Z_i}^2}$ and the coupling $g_{Z_i WW} = g_{CW} \mathcal{O}_{1i}$.

- Similarly, one can obtain the decay width for $Z_i \rightarrow W'^p W'^m$ process as

$$\Gamma(Z_i \rightarrow W'^p W'^m) = \frac{g_{Z_i W' W'}^2 M_{Z_i}}{192\pi r_{iW'}^2} (1 - 4r_{iW'})^{3/2} \left(1 + 20r_{iW'} + 12r_{iW'}^2\right), \quad (\text{B3})$$

where $r_{iW'} = \frac{M_{W'}^2}{M_{Z_i}^2}$ and the coupling $g_{Z_i W' W'} = g_H \mathcal{O}_{2i}$.

- The new neutral gauge boson Z_i can also decay into pair of scalar dark matter candidate in this model. The decay width for this process $Z_i \rightarrow DD^*$ is given by [66]

$$\Gamma(Z_i \rightarrow DD^*) = \frac{g_{Z_i DD}^2 M_{Z_i}}{48\pi} (1 - 4r_{iD})^{3/2}, \quad (\text{B4})$$

where the coupling $g_{Z_i DD} = g_H \mathcal{O}_{2i}$ and $r_{iD} = \frac{M_D^2}{M_{Z_i}^2}$. We note that D is a triplet-like scalar dark matter in this model and we assumed this dark matter doesn't mix with other scalars in this calculation.

- The decay width for $Z_i \rightarrow H^+ H^-$ is given by

$$\Gamma(Z_i \rightarrow H^+ H^-) = \frac{g_{Z_i H^+ H^-}^2 M_{Z_i}}{48\pi} (1 - 4r_{iH^\pm})^{3/2}, \quad (\text{B5})$$

where $r_{iH^\pm} = \frac{M_{H^\pm}^2}{M_{Z_i}^2}$ and the coupling $g_{Z_i H^+ H^-}$ is given as follows

$$g_{Z_i H^+ H^-} = \frac{1}{2}(c_W g - s_W g') \mathcal{O}_{1i} - \frac{1}{2}g_H \mathcal{O}_{2i} + g_X \mathcal{O}_{3i}. \quad (\text{B6})$$

- The decay width for $Z_i \rightarrow Z_j H$ is given by [66]

$$\begin{aligned} \Gamma(Z_i \rightarrow Z_j H) &= \frac{g_{Z_i Z_j H}^2 M_{Z_i}}{192\pi M_{Z_j}^2} \left(1 + (r_{ij} - r_{iH})^2 - 2(r_{ij} + r_{iH})\right)^{1/2} \\ &\quad \times \left(1 + (r_{ij} - r_{iH})^2 + 10r_{ij} - 2r_{iH}\right), \end{aligned} \quad (\text{B7})$$

where $r_{iH} = \frac{M_H^2}{M_{Z_i}^2}$, $r_{ij} = \frac{M_{Z_j}^2}{M_{Z_i}^2}$ and the coupling $g_{Z_i Z_j H}$ is given as follows

$$\begin{aligned} g_{Z_i Z_j H} &= \frac{v}{2} \left((c_W g + s_W g') \mathcal{O}_{1j} - g_H \mathcal{O}_{2j} - 2g_X \mathcal{O}_{3j} \right) \\ &\quad \times \left((c_W g + s_W g') \mathcal{O}_{1i} - g_H \mathcal{O}_{2i} - 2g_X \mathcal{O}_{3i} \right), \end{aligned} \quad (\text{B8})$$

here v is the VEV of the SM Higgs field. Note that we have ignored the mixing of SM like-Higgs H with other scalar bosons in the above calculations.

- Finally, if not kinematically prohibited, the new neutral gauge bosons can also decay into W' and the dark matter D . The decay width for this process can be computed as

$$\Gamma(Z_i \rightarrow W'^p D^* / W'^m D) = \frac{g_{Z_i W' D}^2 M_{Z_i}}{192\pi M_{W'}^2} \left(1 + (r_{iW'} - r_{iD})^2 - 2(r_{iW'} + r_{iD})\right)^{1/2} \times \left(1 + (r_{iW'} - r_{iD})^2 + 10r_{iW'} - 2r_{iD}\right), \quad (\text{B9})$$

where the coupling $g_{Z_i W' D} = g_H^2 \mathcal{O}_{2i} v_\Delta$ with v_Δ being the VEV of $SU(2)_H$ triplet Higgs.

In Figs. 10 and 11, we show the scatter plots of the ratio of decay width over mass of the two new gauge bosons in the heavy M_X and light M_X scenarios respectively. In those plots, we set the dark matter mass M_D to be 10% of the new heavy neutral gauge boson Z_i (*i.e.* $M_D = 0.1 \times M_{Z_2}$ in the case of heavy M_X scenario, while $M_D = 0.1 \times M_{Z_3}$ in the case of light M_X scenario), charged Higgs mass M_{H^\pm} equals 1.5 TeV and the mass of $W'^{(p,m)}$ is randomly chosen in the range of $[M_D, 200 \text{ TeV}]$. Moreover, we assume the masses of new heavy fermions are degenerate and equal to 3 TeV. We note that v_Δ can be derived from other parameters according to $v_\Delta = 0.5 \sqrt{\frac{4M_{W'}^2}{g_H^2} - (v^2 + v_\Phi^2)}$. From these scatter plots one can see that for the heavy neutral gauge bosons in both scenarios, their ratios Γ_{Z_i}/M_{Z_i} are all below $\sim 1\%$, until they are heavier than 10 TeV the ratios can then reach $\sim 6\%$. However for the light Z_1 in the light M_X scenario, Γ_{Z_1}/M_{Z_1} is well below 10^{-4} .

-
- [1] A. Salam and J. C. Ward, “Weak and electromagnetic interactions,” *Nuovo Cim.* **11**, 568 (1959). doi:10.1007/BF02726525
- [2] S. L. Glashow, “Partial Symmetries of Weak Interactions,” *Nucl. Phys.* **22**, 579 (1961). doi:10.1016/0029-5582(61)90469-2
- [3] S. Weinberg, “A Model of Leptons,” *Phys. Rev. Lett.* **19**, 1264 (1967). doi:10.1103/PhysRevLett.19.1264
- [4] A. Salam (1968). N. Svartholm, ed. *Elementary Particle Physics: Relativistic Groups and Analyticity. Eighth Nobel Symposium.* Stockholm: Almqvist and Wiksell. p. 367.
- [5] F. Englert and R. Brout, “Broken Symmetry and the Mass of Gauge Vector Mesons,” *Phys. Rev. Lett.* **13**, 321 (1964). doi:10.1103/PhysRevLett.13.321
- [6] P. W. Higgs, “Broken Symmetries and the Masses of Gauge Bosons,” *Phys. Rev. Lett.* **13**, 508 (1964). doi:10.1103/PhysRevLett.13.508
- [7] G. S. Guralnik, C. R. Hagen and T. W. B. Kibble, “Global Conservation Laws and Massless Particles,” *Phys. Rev. Lett.* **13**, 585 (1964). doi:10.1103/PhysRevLett.13.585
- [8] For a recent review on dark matter, see T. Lin, “TASI lectures on dark matter models and direct detection,” arXiv:1904.07915 [hep-ph] and references therein.
- [9] For a review on dark energy, see for example P. J. E. Peebles and B. Ratra, “The Cosmological constant and dark energy,” *Rev. Mod. Phys.* **75**, 559 (2003) doi:10.1103/RevModPhys.75.559 [astro-ph/0207347] and references therein.
- [10] See for example the textbook by S. Dodelson, “*Modern Cosmology*,” Amsterdam, Netherlands: Academic Pr. (2003).
- [11] W. C. Huang, Y. L. S. Tsai and T. C. Yuan, “G2HDM : Gauged Two Higgs Doublet Model,” *JHEP* **1604**, 019 (2016) doi:10.1007/JHEP04(2016)019 [arXiv:1512.00229 [hep-ph]].

- [12] N. G. Deshpande and E. Ma, “Pattern of symmetry breaking with two Higgs doublets,” *Phys. Rev. D* **18**, 2574 (1978). doi:10.1103/PhysRevD.18.2574
- [13] E. Ma, “Verifiable radiative seesaw mechanism of neutrino mass and dark matter,” *Phys. Rev. D* **73**, 077301 (2006) doi:10.1103/PhysRevD.73.077301 [hep-ph/0601225].
- [14] R. Barbieri, L. J. Hall, and V. S. Rychkov, “Improved naturalness with a heavy Higgs: An alternative road to LHC physics,” *Phys. Rev. D* **74**, 015007 (2006) doi:10.1103/PhysRevD.74.015007 [hep-ph/0603188].
- [15] L. Lopez Honorez, E. Nezri, J. F. Oliver, and M. H. G. Tytgat, “The inert doublet model: An archetype for dark matter,” *JCAP* **02**, 028 (2007) doi:10.1088/1475-7516/2007/02/028 [hep-ph/0612275].
- [16] G. C. Branco, P. M. Ferreira, L. Lavoura, M. N. Rebelo, M. Sher, and J. P. Silva, “Theory and phenomenology of two-Higgs-doublet models,” *Phys. Rep.* **516**, 1 (2012) doi:10.1016/j.physrep.2012.02.002 [arXiv:1106.0034 [hep-ph]].
- [17] A. Arhrib, Y. L. S. Tsai, Q. Yuan, and T. C. Yuan, “An updated analysis of inert Higgs doublet model in light of the recent results from LUX, PLANCK, AMS-02 and LHC,” *JCAP* **06** (2014) 030 doi:10.1088/1475-7516/2014/06/030 [arXiv:1310.0358 [hep-ph]].
- [18] A. Arhrib, R. Benbrik and T. C. Yuan, “Associated Production of Higgs at Linear Collider in the Inert Higgs Doublet Model,” *Eur. Phys. J. C* **74**, 2892 (2014) doi:10.1140/epjc/s10052-014-2892-5 [arXiv:1401.6698 [hep-ph]].
- [19] A. Ilnicka, M. Krawczyk, and T. Robens, “Inert doublet model in light of LHC Run I and astrophysical data,” *Phys. Rev. D* **93**, no. 5, 055026 (2016) doi:10.1103/PhysRevD.93.055026 [arXiv:1508.01671 [hep-ph]].
- [20] A. Belyaev, G. Cacciapaglia, I. P. Ivanov, F. Rojas-Abatte, and M. Thomas, “Anatomy of the inert two Higgs doublet model in the light of the LHC and non-LHC dark matter searches,” *Phys. Rev. D* **97**, no. 3, 035011 (2018) doi:10.1103/PhysRevD.97.035011 [arXiv:1612.00511 [hep-ph]].

- [21] B. Eiteneuer, A. Goudelis, and J. Heisig, “The inert doublet model in the light of Fermi-LAT gamma-ray data: a global fit analysis,” *Eur. Phys. J. C* **77**, no. 9, 624 (2017) doi:10.1140/epjc/s10052-017-5166-1 [arXiv:1705.01458 [hep-ph]].
- [22] D. Borah, P. S. B. Dev and A. Kumar, “TeV scale leptogenesis, inflaton dark matter and neutrino mass in a scotogenic model,” *Phys. Rev. D* **99**, no. 5, 055012 (2019) doi:10.1103/PhysRevD.99.055012 [arXiv:1810.03645 [hep-ph]].
- [23] T. W. Kephart and T. C. Yuan, “Origins of inert Higgs doublets,” *Nucl. Phys.* **B906**, 549 (2016) doi:10.1016/j.nuclphysb.2016.03.023 [arXiv:1508.00673 [hep-ph]].
- [24] A. Goudelis, B. Herrmann and O. Stål, “Dark matter in the Inert Doublet Model after the discovery of a Higgs-like boson at the LHC,” *JHEP* **1309**, 106 (2013) doi:10.1007/JHEP09(2013)106 [arXiv:1303.3010 [hep-ph]].
- [25] B. Swiezewska and M. Krawczyk, “Diphoton rate in the inert doublet model with a 125 GeV Higgs boson,” *Phys. Rev. D* **88**, no. 3, 035019 (2013) doi:10.1103/PhysRevD.88.035019 [arXiv:1212.4100 [hep-ph]].
- [26] A. Arhrib, R. Benbrik and N. Gaur, “ $H \rightarrow \gamma\gamma$ in Inert Higgs Doublet Model,” *Phys. Rev. D* **85**, 095021 (2012) doi:10.1103/PhysRevD.85.095021 [arXiv:1201.2644 [hep-ph]].
- [27] L. M. Krauss and F. Wilczek, “Discrete Gauge Symmetry in Continuum Theories,” *Phys. Rev. Lett.* **62**, 1221 (1989). doi:10.1103/PhysRevLett.62.1221
- [28] R. Kallosh, A. D. Linde, D. A. Linde, and L. Susskind, “Gravity and global symmetries,” *Phys. Rev. D* **52**, 912 (1995) doi:10.1103/PhysRevD.52.912 [hep-th/9502069].
- [29] C. R. Chen, Y. X. Lin, C. S. Nugroho, R. Ramos, Y. L. S. Tsai and T. C. Yuan, in preparation.
- [30] C. R. Chen, Y. X. Lin, V. Q. Tran and T. C. Yuan, “Pair production of Higgs bosons at the LHC in gauged 2HDM,” *Phys. Rev. D* **99**, no. 7, 075027 (2019) doi:10.1103/PhysRevD.99.075027 [arXiv:1810.04837 [hep-ph]].

- [31] A. Arhrib, W. C. Huang, R. Ramos, Y. L. S. Tsai and T. C. Yuan, “Consistency of a gauged two-Higgs-doublet model: Scalar sector,” *Phys. Rev. D* **98**, no. 9, 095006 (2018) doi:10.1103/PhysRevD.98.095006 [arXiv:1806.05632 [hep-ph]].
- [32] P. Ko, Y. Omura and C. Yu, “A Resolution of the Flavor Problem of Two Higgs Doublet Models with an Extra $U(1)_H$ Symmetry for Higgs Flavor,” *Phys. Lett. B* **717**, 202 (2012) doi:10.1016/j.physletb.2012.09.019 [arXiv:1204.4588 [hep-ph]].
- [33] M. D. Campos, D. Cogollo, M. Lindner, T. Melo, F. S. Queiroz and W. Rodejohann, “Neutrino Masses and Absence of Flavor Changing Interactions in the 2HDM from Gauge Principles,” *JHEP* **1708**, 092 (2017) doi:10.1007/JHEP08(2017)092 [arXiv:1705.05388 [hep-ph]].
- [34] D. A. Camargo, L. Delle Rose, S. Moretti and F. S. Queiroz, “Collider bounds on 2-Higgs doublet models with $U(1)_X$ gauge symmetries,” *Phys. Lett. B* **793**, 150 (2019) doi:10.1016/j.physletb.2019.04.048 [arXiv:1805.08231 [hep-ph]].
- [35] D. A. Camargo, A. G. Dias, T. B. de Melo and F. S. Queiroz, “Neutrino Masses in a Two Higgs Doublet Model with a $U(1)$ Gauge Symmetry,” *JHEP* **1904**, 129 (2019) doi:10.1007/JHEP04(2019)129 [arXiv:1811.05488 [hep-ph]].
- [36] D. A. Camargo, M. D. Campos, T. B. de Melo and F. S. Queiroz, “A Two Higgs Doublet Model for Dark Matter and Neutrino Masses,” arXiv:1901.05476 [hep-ph].
- [37] D. Cogollo, R. D. Matheus, T. B. de Melo and F. S. Queiroz, “Type I + II Seesaw in a Two Higgs Doublet Model,” arXiv:1904.07883 [hep-ph].
- [38] W. C. Huang, H. Ishida, C. T. Lu, Y. L. S. Tsai and T. C. Yuan, “Signals of New Gauge Bosons in Gauged Two Higgs Doublet Model,” *Eur. Phys. J. C* **78**, no. 8, 613 (2018) doi:10.1140/epjc/s10052-018-6067-7 [arXiv:1708.02355 [hep-ph]].
- [39] W. C. Huang, Y. L. S. Tsai and T. C. Yuan, “Gauged Two Higgs Doublet Model confronts the LHC 750 GeV diphoton anomaly,” *Nucl. Phys. B* **909**, 122 (2016) doi:10.1016/j.nuclphysb.2016.05.002 [arXiv:1512.07268 [hep-ph]].

- [40] CEPC-SPPC Study Group, “CEPC-SPPC Preliminary Conceptual Design Report. 1. Physics and Detector,” IHEP-CEPC-DR-2015-01, IHEP-TH-2015-01, IHEP-EP-2015-01.
- [41] P. Q. Hung, “A Model of electroweak-scale right-handed neutrino mass,” *Phys. Lett. B* **649**, 275 (2007) doi:10.1016/j.physletb.2007.03.067 [hep-ph/0612004].
- [42] H. Ruegg and M. Ruiz-Altaba, “The Stüeckelberg field,” *Int. J. Mod. Phys. A* **19**, 3265 (2004) doi:10.1142/S0217751X04019755 [hep-th/0304245].
- [43] M. Tanabashi *et al.* [Particle Data Group], “Review of Particle Physics,” *Phys. Rev. D* **98**, no. 3, 030001 (2018). doi:10.1103/PhysRevD.98.030001
- [44] B. Kors and P. Nath, “Aspects of the Stüeckelberg extension,” *JHEP* **0507**, 069 (2005) doi:10.1088/1126-6708/2005/07/069 [hep-ph/0503208].
- [45] B. Kors and P. Nath, “How Stüeckelberg extends the standard model and the MSSM,” doi:10.1142/9789812701756_0056 hep-ph/0411406.
- [46] B. Kors and P. Nath, “A Supersymmetric Stüeckelberg U(1) extension of the MSSM,” *JHEP* **0412**, 005 (2004) doi:10.1088/1126-6708/2004/12/005 [hep-ph/0406167].
- [47] B. Kors and P. Nath, “A Stüeckelberg extension of the standard model,” *Phys. Lett. B* **586**, 366 (2004) doi:10.1016/j.physletb.2004.02.051 [hep-ph/0402047].
- [48] D. Feldman, Z. Liu and P. Nath, “The Stüeckelberg extension and milli weak and milli charged dark matter,” *AIP Conf. Proc.* **939**, 50 (2007) doi:10.1063/1.2803786 [arXiv:0705.2924 [hep-ph]].
- [49] D. Feldman, Z. Liu and P. Nath, “The Stüeckelberg Z-prime Extension with Kinetic Mixing and Milli-Charged Dark Matter From the Hidden Sector,” *Phys. Rev. D* **75**, 115001 (2007) doi:10.1103/PhysRevD.75.115001 [hep-ph/0702123 [HEP-PH]].
- [50] D. Feldman, Z. Liu and P. Nath, “The Stüeckelberg Z Prime at the LHC: Discovery Potential, Signature Spaces and Model Discrimination,” *JHEP* **0611**, 007 (2006) doi:10.1088/1126-6708/2006/11/007 [hep-ph/0606294].

- [51] J. Erler and P. Langacker, “Electroweak model and constraints on new physics,” hep-ph/0407097.
- [52] S. Schael *et al.* [ALEPH and DELPHI and L3 and OPAL and SLD Collaborations and LEP Electroweak Working Group and SLD Electroweak Group and SLD Heavy Flavour Group], “Precision electroweak measurements on the Z resonance,” Phys. Rept. **427**, 257 (2006) doi:10.1016/j.physrep.2005.12.006 [hep-ex/0509008].
- [53] U. Baur, O. Brein, W. Hollik, C. Schappacher and D. Wackerroth, “Electroweak radiative corrections to neutral current Drell-Yan processes at hadron colliders,” Phys. Rev. D **65**, 033007 (2002) doi:10.1103/PhysRevD.65.033007 [hep-ph/0108274].
- [54] S. Schael *et al.* [ALEPH and DELPHI and L3 and OPAL and LEP Electroweak Collaborations], “Electroweak Measurements in Electron-Positron Collisions at W-Boson-Pair Energies at LEP,” Phys. Rept. **532**, 119 (2013) doi:10.1016/j.physrep.2013.07.004 [arXiv:1302.3415 [hep-ex]].
- [55] M. Aaboud *et al.* [ATLAS Collaboration], “Search for new high-mass phenomena in the dilepton final state using 36 fb^{-1} of proton-proton collision data at $\sqrt{s} = 13 \text{ TeV}$ with the ATLAS detector,” JHEP **1710**, 182 (2017) doi:10.1007/JHEP10(2017)182 [arXiv:1707.02424 [hep-ex]].
- [56] M. Aaboud *et al.* [ATLAS Collaboration], “Measurement of the cross-section for electroweak production of dijets in association with a Z boson in pp collisions at $\sqrt{s} = 13 \text{ TeV}$ with the ATLAS detector,” Phys. Lett. B **775**, 206 (2017) doi:10.1016/j.physletb.2017.10.040 [arXiv:1709.10264 [hep-ex]].
- [57] G. Aad *et al.* [ATLAS Collaboration], “Search for high-mass dilepton resonances using 139 fb^{-1} of pp collision data collected at $\sqrt{s} = 13 \text{ TeV}$ with the ATLAS detector,” arXiv:1903.06248 [hep-ex].
- [58] J. Alwall *et al.*, “The automated computation of tree-level and next-to-leading order differential cross sections, and their matching to parton shower simulations,” JHEP

- 1407**, 079 (2014) doi:10.1007/JHEP07(2014)079 [arXiv:1405.0301 [hep-ph]].
- [59] F. Feroz, M. P. Hobson and M. Bridges, “MultiNest: an efficient and robust Bayesian inference tool for cosmology and particle physics,” *Mon. Not. Roy. Astron. Soc.* **398**, 1601 (2009) doi:10.1111/j.1365-2966.2009.14548.x [arXiv:0809.3437 [astro-ph]].
- [60] K. Fujii *et al.*, “Physics Case for the 250 GeV Stage of the International Linear Collider,” arXiv:1710.07621 [hep-ex].
- [61] D. d’Enterria, “Physics case of FCC-ee,” *Frascati Phys. Ser.* **61**, 17 (2016) [arXiv:1601.06640 [hep-ex]].
- [62] S. Martellotti, “The NA62 Experiment at CERN,” arXiv:1510.00172 [physics.ins-det].
- [63] T. Aushev *et al.*, “Physics at Super B Factory,” arXiv:1002.5012 [hep-ex].
- [64] S. Alekhin *et al.*, “A facility to Search for Hidden Particles at the CERN SPS: the SHiP physics case,” *Rept. Prog. Phys.* **79**, no. 12, 124201 (2016) doi:10.1088/0034-4885/79/12/124201 [arXiv:1504.04855 [hep-ph]].
- [65] A. Pilaftsis and C. E. M. Wagner, “Higgs bosons in the minimal supersymmetric standard model with explicit CP violation,” *Nucl. Phys. B* **553**, 3 (1999) doi:10.1016/S0550-3213(99)00261-8 [hep-ph/9902371].
- [66] V. D. Barger and K. Whisnant, “Heavy Z Boson Decays to Two Bosons in $E(6)$ Superstring Models,” *Phys. Rev. D* **36** (1987) 3429. doi:10.1103/PhysRevD.36.3429